

# Chapter 3

## Melt Extracted Microwires

H. Wang, F.X. Qin, H.X. Peng, and J.F. Sun

### 3.1 Introduction to Melt Extraction Technique

Amorphous microwires as a new category of advanced materials possess many excellent mechanical and magnetic properties, and have received considerable attention from both the research and industry community. Significant efforts have been devoted to the optimization of fabrication process, tailoring of mechanical and magnetic properties, sensor and microwave applications [1–6]. To now, amorphous wires can be prepared by several methods such as glass coating (Taylor-wire technique) [7, 8], in-water quenching [9–12], and melt extraction technology (MET) [13–16]. Compared with others, the solidification rate of wires prepared by melt extraction is the highest, which endows the resultant wires many excellent mechanical and magnetic properties. To our best recollection, there is no dedicated monograph on melt extraction microwires yet. Therefore, in this chapter, we will focus on the melt-extracted amorphous microwires, detailing the fabrication process, wire formation mechanism, mechanical and magnetic properties, thus provide some technical base for its application in sensor and multifunctional composites.

The concept of melt extraction was firstly introduced by Maringer [17] in 1974 to produce metallic microwires. The basic principle can be briefed as follows: a high-speed wheel with a sharp edge is employed to contact the molten alloy surface and then a molten layer can be rapidly extracted and cooled down to be form of wires. During the extraction process, the solidification rate of metallic wires can

---

H. Wang • F.X. Qin (✉) • H.X. Peng

Institute for Composites Science Innovation (InCSI), School of Materials Science and Engineering, Zhejiang University, Hangzhou 310027, China  
e-mail: [faxiangqin@zju.edu.cn](mailto:faxiangqin@zju.edu.cn)

J.F. Sun

School of Materials Science and Engineering, Harbin Institute of Technology, Harbin 150001, China

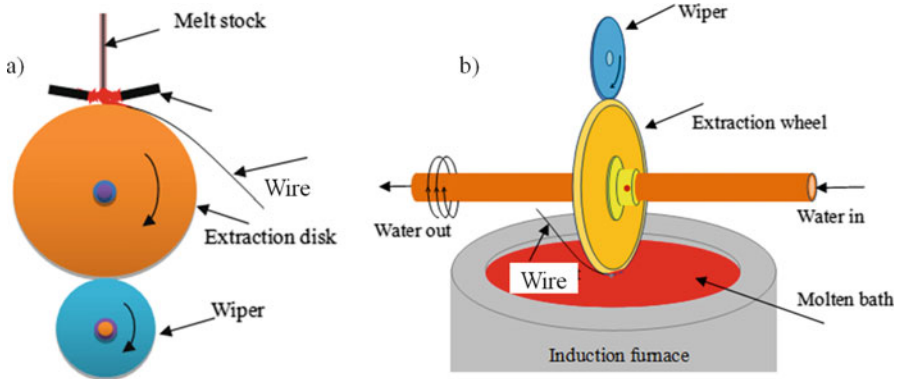


**Fig. 3.1** Schematic illustrations of melt extraction technique, (a) pendant drop and (b) crucible melt extraction method

reach up to  $10^5$ – $10^6$  K/s; it has been widely used to fabricate amorphous metallic wires and a few ceramic microwires, e.g.,  $\text{CaO}/\text{Al}_2\text{O}_3$  and  $\text{Al}_2\text{O}_3/\text{Y}_2\text{O}_3$  [18–20]. Because it does not require any liquid cooling mediums, MET can also be used to fabricate some highly reactive alloys such as aluminum, titanium, zirconium, and magnesium wires [13, 21, 22]. Melt extraction technique was divided into pendant drop melt extraction (PDME) [23–25] and crucible melt extraction (CME) [13, 15, 22, 26] according to the source of molten materials, as shown in Fig. 3.1. For PDME (Fig. 3.1a), the source of molten material is a droplet formed on the end of master alloy, the liquid metal solidifies on the extracted wheel edge and then releases spontaneously in the form of solidified microwires. There is no reaction between crucible and melt during the fabrication process. However, the alloy was melted by oxy-acetylene flame which will lead to the oxidation of solidified microwires, meanwhile, the molten drop was hanged in the air and sensitive to ambient environment such as the oxy-acetylene flame and rotation of wheel will result in the molten instability. The CME facility is schematically shown in Fig. 3.1b. Unlike PDME, the master alloy was put in a crucible below the metal wheel and remelted by induction heating. The diameter of the fabricated microwires was controlled by adjusting the extracted wheel speed and the insert depth between the wheel and melt. By reducing the size of the crucible, ultra fine, ultra soft magnetic and high reactive metallic and amorphous microwires, for example, Co-based, Fe-based, Ti-based, Al-based, and  $\text{CaO}-\text{Al}_2\text{O}_3-\text{ZrO}_2$  wires were fabricated in McGill University [18, 26–31] and Tohoku University [32–34] over the last few decades.

### 3.2 Casting Method: Production and Processing

Melt extraction requires bringing the liquid metal puddle into contact with a V-shaped rotating wheel edge. The metal solidifies on the edge, adheres, and then releases in the form of solid powder, wire, or microwire depending on the process

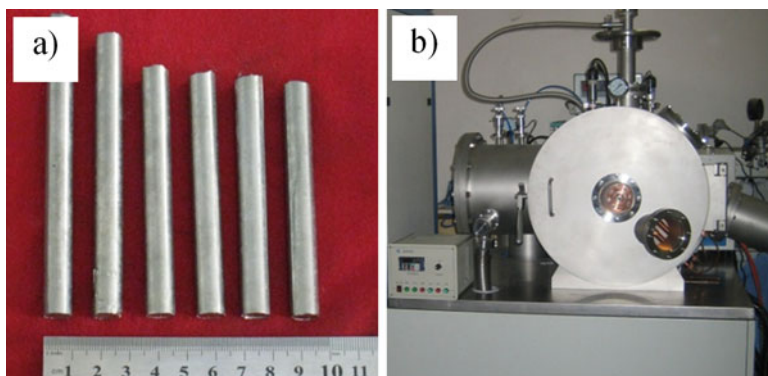


**Fig. 3.2** (a) Quaternary alloy ingots and (b) overview of melt extraction setup

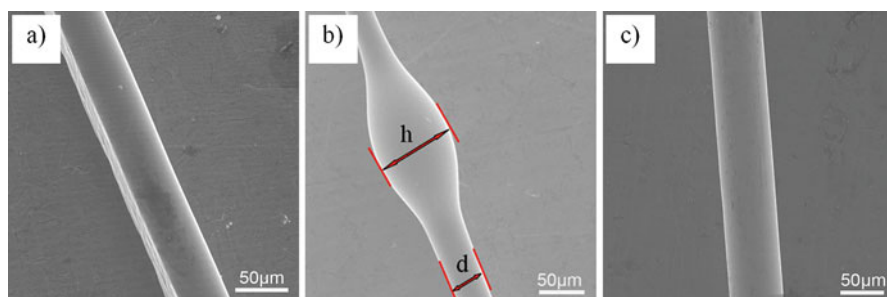


**Fig. 3.3** SEM images of the melt-extracted microwires showing (a) uniform with concaved track wire; (b) wire with Rayleigh waves; (c) fine and uniform wire

parameters, viscosity of the melts and the wettability between molten and extracted wheel. The ingot with a diameter of 8–10 mm was prepared in argon atmosphere by arc melting, as shown in Fig. 3.2a. Processing optimization was performed using a home-built crucible melt extraction facility using a copper wheel with diameter of 160 mm and 60° knife-edge (Fig. 3.2b).

### 3.2.1 Process Parameter and Optimization

During the optimization of different melt extraction process parameters, wires of three different geometrical morphologies are obtained: one is uniform wire but with concaved track, the second is wire with Rayleigh waves, and the third is fine and uniform wire, as shown in Fig. 3.3a–c, respectively. The diameter of the uniform circular part of wires and the thickness of the nonuniform part of Rayleigh waves are defined as  $d$  and  $h$ , respectively, as shown in Fig. 3.3b. The dimensions of wires,

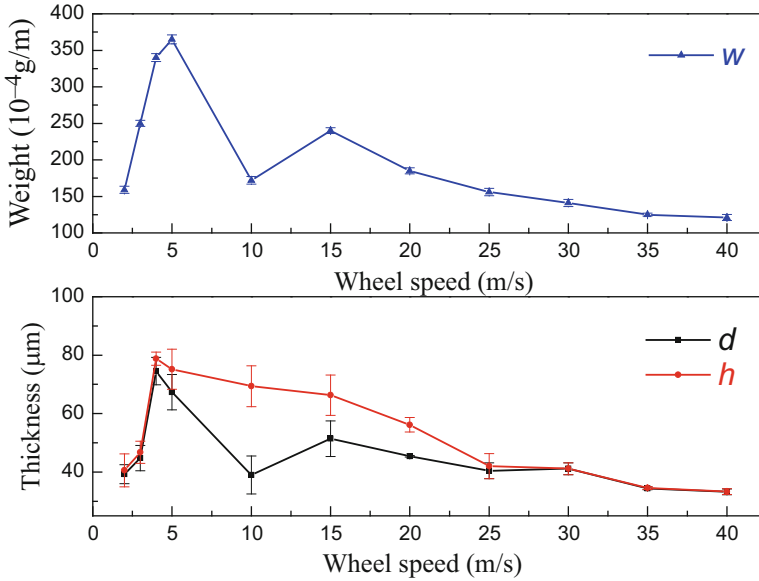


**Fig. 3.4** The weight per meter  $w$ , wire diameter  $d$ , Rayleigh wave thickness  $h$  as a function of wheel velocity

i.e.,  $d$  and  $h$ , are measured for at least 50 wire samples for SEM images to obtain the average for each data point. The weight of the extracted wires,  $w$ , i.e., extracted layer, was examined for ten samples each with length of 10 cm.

The variation of wire diameters *vs* wheel velocity passes through a maximum and then decreases with the increase of wheel velocity, shown in Fig. 3.4. For the weight of the extracted wires, the minimum of  $w$  occurs at a wheel velocity of 10 m/s, where the gap between  $d$  and  $h$  reaches maximum. These two plots can be divided into three regions according to the wheel speed: (a) low-speed region (2–5 m/s), (b) intermediate speed region (5–30 m/s), and (c) high-speed region (30–40 m/s). At low- and high-speed regions, wires exhibit a uniform diameter; while in the medium region, Rayleigh waves are found and  $h$  decreases with an increase of the wheel velocity. Obviously, there are some fluctuations of  $d$ ,  $h$ , and  $w$  in the medium region. With an increase in wheel velocity, Rayleigh waves form and become larger; i.e., the difference between  $d$  and  $h$  increases and reaches a maximum at a wheel velocity of 10 m/s, where a larger number of particles formed.

It was considered previously that the diameter of the wires or the thickness of the ribbon decreases with the increase of the wheel velocity, but in our test, the result is abnormal at low speeds. This phenomenon was also found in the melt extraction of ceramic material by Allahverdi [29] and Taha [35] in the melt spinning process of Al-Cu alloy. The abnormal behavior at low velocity may be caused by increasing wheel vibration when the wheel velocity increases within the low-speed range. The deeper the wheel penetrates into the molten, the larger the

diameters will be. On the other hand, as the wheel velocity increases (less than 10 m/s), the concave tracks on the extracted wire become wider. Therefore, the increasing vibration is the most likely reason for this abnormal behavior. With the increasing velocity ( $V_s > 10$  m/s), the Rayleigh waves become smaller and the thickness of the wires decreases. The formation of the Rayleigh waves can be found elsewhere [36–38]. In the high-speed region ( $V_s > 30$  m/s), fine and uniform wires with a diameter of less than 40  $\mu\text{m}$  are obtained. The production of high-quality wires in the high-speed region has been reported by A. Inoue [39] for the melt extraction of Fe-Si-B and Co-Si-B alloys.

The Rayleigh instability is well known for a jet of liquid. Surface tension destabilizes the jet stream, and finally breaks it up into fine droplets. In the melt extraction process, since heat transfer and supercooling are simultaneously occurring with the extraction, the destabilizing effect of the surface tension cannot readily result in the wire or the stream may even break up. Hence, wires can be obtained, and frozen Rayleigh waves are observed on the free surface of the extracted wires, as illustrated by Allahverdi et al. [40] in Amorphous  $\text{CaO-Al}_2\text{O}_3$  wire extraction (Fig. 3.5).

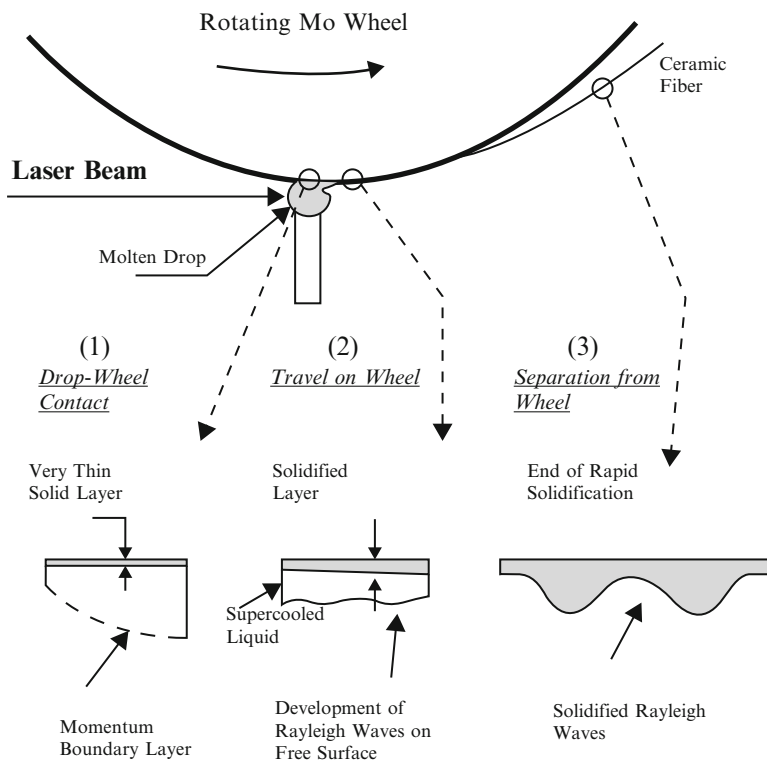


**Fig. 3.5** Schematic of supercooled liquid layer evolution for wires exhibiting Rayleigh waves

The molten feed rate together with the wheel velocity affects the roundness of the wire and the formation of Rayleigh waves obviously. The faster the molten feeds, the thicker it immerses into the copper wheel, which promoted heat transformed into it. When it happened, the molten supercooled below the melting point, and solidification occurred adjacent to the wheel tip, leading to the formation of the concave; meanwhile, on the free surface of the extracted layer, heat transferred to the supercooled region and surface tension acted as a dominant factor, tending to minimize the surface of the liquid layer, and some Rayleigh waves may occur when it experienced some improper cooling rate. Therefore, the coexistence of concave and Rayleigh waves narrows down the operating window of MET very and limits its applications.

On the other hand, as viscosity and surface tension relate closely to the temperature and superheat degree (difference value between actual temperature and melting point  $T_m$ ) of the melt, they also have effects on the melt-extracted process. Once the melting point of molten alloy is higher than the extracted wheel, melting and hot corrosion of the wheel will happen during the extraction process. As a result, the microstructures and compositions of the microwires had been modified, thereby reducing accuracy of wheel and stability of melt-extracted process. Figure 3.6 shows the TEM micromorphology of Co-based microwires with melting temperature of  $\sim 120$  K above the melting. The microwires show two phases of amorphous state and nano-crystal state ( $\sim 10$  nm) with obvious boundary as displayed in Fig. 3.6a. Compositions of the amorphous and nano-crystal phases are identified by EDS and shown as  $\text{Co}_{89.58}\text{Fe}_{5.43}\text{Si}_{3.87}\text{B}_{1.12}$  and  $\text{Co}_{20.54}\text{Fe}_{1.21}\text{Si}_{1.84}\text{Cu}_{76.41}$ , respectively. The nano-crystal phases were further explored as Cu with FCC structure, which indicates that the rim of Cu wheel was melt caused by excessively high temperature during the melt-extracted process and leads to the changes in compositions and properties of microwires.

According to the processes mentioned above, the optimized parameters of melt-extracted Co-based microwires are listed as follows:

1. Linear velocity of wheel ranged from 25 to 30 m/s;
2. Feeding speed ranged from 60 to 90  $\mu\text{m/s}$ ;
3. The melting temperature determined as  $T_m + 50$  K;
4. Wheel fabricated by pure Cu and preheated at 100  $^\circ\text{C}$ ;
5. The melt-extracted process operated in Ar atmosphere.

We have fabricated Co-based micromicrowires with excellent qualities such as high roundness and good uniformity, the maximum length of an extracted microwire is large than 2000 mm. The micromicrowires so fabricated are displayed in Fig. 3.7.

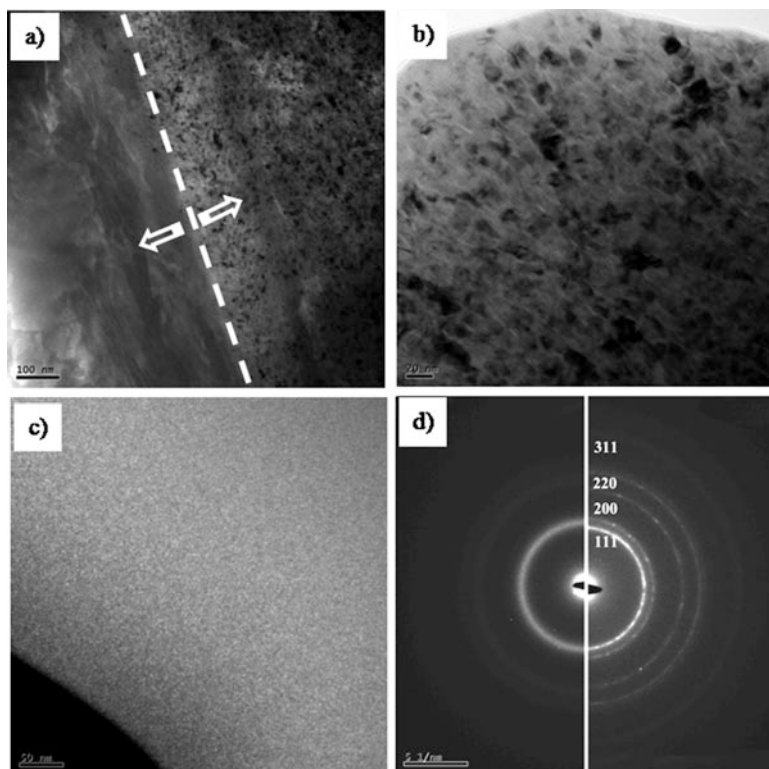


**Fig. 3.6** TEM analyses of the extracted Co-based microwires with high molten temperature (a) TEM analysis of dual phase; (b) nanocrystals; (c) amorphous phase; (d) SAED for the amorphous and nanocrystals structures

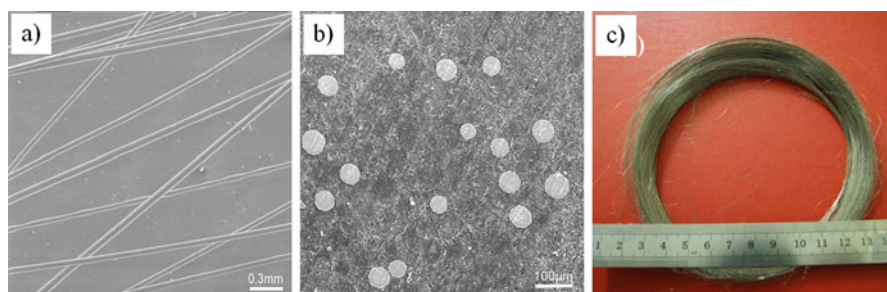


**Fig. 3.7** Images of melt-extracted Co-based microwires (a) Longitudinal image; (b) Cross-section and (c) Macro-morphology

### 3.2.2 Puddle Deformation Behavior

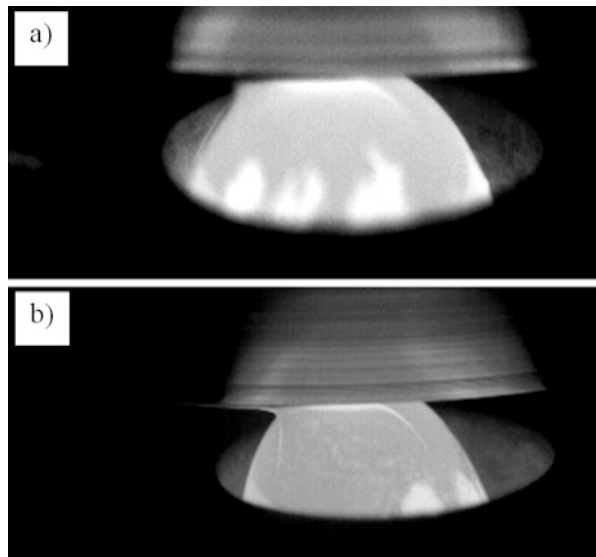
The contact geometry between the tip of the rotary wheel and molten provides us with some insight into the formation mechanism of melt extraction metallic wires. Figure 3.8a, b shows the contact geometry at wheel velocities of 2 and 30 m/s, where uniform wires were fabricated. From Fig. 3.8a, due to the surface tension of the molten materials and the decrease in temperature, the dragged molten tends to shrink with lower energy and a gap is observed in the front of the contact area. As the speed is increased, as shown in Fig. 3.8b, the shear force between the wheel and the molten becomes greater; a sharp frontier was seen in front of the contact area, which plays an important role in the formation of amorphous wires.

In fact, wetting of the copper by molten alloy plays a pivotal role in producing amorphous wires. In an isothermal static wetting, the wettability can be expressed by Young's equation as follows:

$$\cos \theta = (\gamma_{sv} - \gamma_{sl}) / \gamma_{lv} \quad (3.1)$$

where  $\gamma$  is the surface energy or surface tension; and the subscripts  $s, l$ , and  $v$  indicate the solid, liquid, and vapor, respectively. Once the contact interface begins to move, the conditions are generally complicated. This is because the dynamic forces generated by motion change the surface tension, altering the balance in the Young's equation. In the optimization of process parameters, the surface tension of molten acts as a hindrance to limit the fluid of molten and tends to increase as the temperature decreases. In the low velocity region, part of the solidification occurs on the wheel tip and reduces the temperature of the molten.

**Fig. 3.8** Contact geometry between molten drop and rotating wheel (a) 2 m/s; (b) 30 m/s [14]





In this region, surface tension evolving with temperature acts as a dominant force to produce metallic wires. The mechanism of wire formation may be influenced by the heat transfer from the molten to the wheel tip; in the high-speed region, wettability of this process is promoted by dynamic shear force and overcomes the surface tension obstacle. The contact time  $\Delta t \approx 46$  ms at a wheel velocity of 35 m/s, during which short period of time, no solidification occurred as revealed in the high-speed video recorder. In this region, fine and uniform wires with circular cross-section were fabricated, which indicates that the wires were in liquid state upon leaving the molten before the solidification completely took place after they were extracted and flew in the argon atmosphere. This is different from the previous result that solidification is almost completed when the extracted layer leaves the wheel during the melt spinning of amorphous ribbons. The accelerated layer is almost liquid, which promoted the momentum penetration into the layer.

During melt extraction, wetting is a dynamic process due to the rotating wheel and there is an additional shear force involved. Moreover, the extraction also includes heat transfer and solidification process. These factors make the puddle and wetting behaviors in the melt extraction process quite distinct. Figure 3.9a shows the contact geometry in extraction process,  $L_c$  and  $\delta$  are the contact length and the thickness of the extracted layer, respectively. In this dynamic state, the wheel tip is moving and a shear force is applied which is due to drag forces at the wheel/liquid interface. Figure 3.9b gives the changes of  $L_c$  and  $\delta$  versus extracted wheel speed. The contact length increases gradually with the wheel speed, while the thickness of the extracted layer decreases rapidly till a wheel velocity of 5 m/s prior to a gradual increase.

With reference to Eq. (3.1), it seems any term that is capable of increasing the numerator of Eq. (3.1), i.e.  $(\gamma_{sv} - \gamma_{sl})$ , or decreases the denominator  $\gamma_{lv}$ , would be able to improve the wetting behavior. Shear force generated during extraction process increases the numerator because it spreads the droplet on the wheel tip and decreases the apparent downstream contact angle. The variation of contact angle, as a result of shear stress, is similar to the hysteresis of contact angle of a drop on an inclined surface.

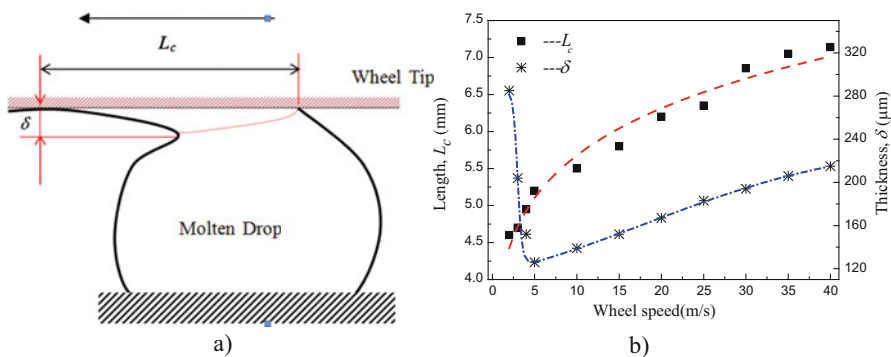


**Fig. 3.9** Schematic illustration of the contact geometry (a) and the evolution of  $L_c$ ,  $\delta$  versus wheel velocity (b)

### 3.2.3 Wires Formation Mechanism

The possible modes of the small-sized metallic samples formation have been described by Kavesh [41] and can fall into the following two mechanisms: (I) thermal transport controlling, (II) momentum transport controlling. According to the boundary layer theory of Schlichting [42, 43], these two limiting cases can be discussed as below:

- (I) Thermal transport controlling: If heat propagates much faster than momentum, a solid layer will form at the wheel tip and grow into the liquid puddle. The solid layer will travel with the rotating wheel and a concave will be formed on the wire cross-section.
- (II) Momentum transport controlling: In this reverse case, the momentum transfer is much faster than the thermal transfer, a liquid layer will be dragged out of the puddle by the rotating wheel to solidify further downstream. When the liquid stream is divorced from the wheel tip, high circular wires are thus produced.

Schlichting has performed an analysis and showed that the depth of the thermal boundary layer  $\delta_t$  and momentum layer  $\delta_u$  in the liquid near the solid boundary is given by:

$$\delta_t \propto L_c / (\text{Pr} \cdot \text{Re})^{0.5}, \quad (3.2)$$

$$\delta_u \propto L_c / \text{Re}^{0.5}, \quad (3.3)$$

where  $L_c$  is the contact length of the extracted layer, and Pr is the Prandtl number of the liquid, and Re is the Reynolds number of the liquid. We can then obtain the correlation between  $\delta_t$  and  $\delta_u$ :

$$\delta_t / \delta_u \propto 1 / \text{Pr} \quad (3.4)$$

For the metallic liquid,  $\text{Pr} \ll 1$ , and we can see that  $\delta_t \gg \delta_u$ , wire dimension is determined by the heat transfer. Based on the IR measurement for the cooling rate in the puddle, it was concluded that almost the ideal cooling conditions exist with a heat transfer coefficient in excess of  $10^6 \text{ W/m}^2\text{K}$ . Outside the puddle, the cooling rates decrease substantially to  $10^4 \text{ W/m}^2\text{K}$ . The ideal cooling conditions on the puddle area suggest that the mechanism of wire formation is controlled by thermal transport rather than momentum transport. However, Sun and Davies believed that the assumption of the ideal cooling region at puddle–substrate interface is unrealistic. They stated that both the thermal and momentum transports control the wire formation mechanism. There are still several discrepancies, and it seems both the thermal and momentum transport mechanisms involved in the wire formation depend on the selected processing parameters.

The unique structure and property correlates closely with its cooling experience during wire formation melt extraction process. However, owing to the typically minor deformation puddle, the limited dwell time, and the high rotation velocity of

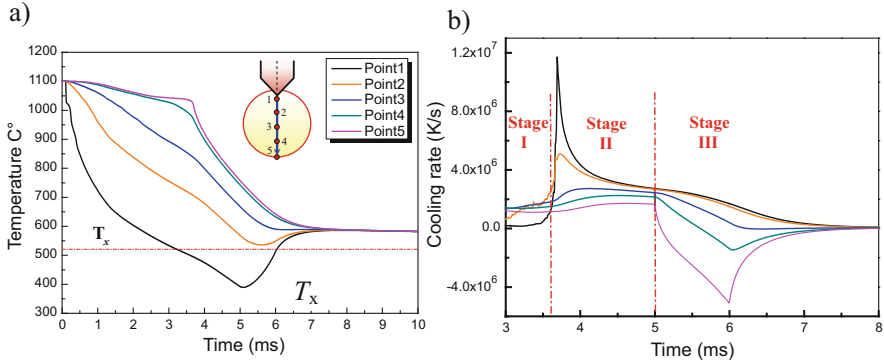


**Fig. 3.10** Temperature and cooling rate distribution at different testing points (a) temperature distribution; (b) cooling rate profile [44]

the wheel in a MET process, it is rather difficult to investigate the process experimentally. In order to establish the correlation between temperature distributions i.e., the cooling rate and microstructure evolution during extraction process, a finite element analysis (FEA) was conducted in a ProCAST™ software. Figure 3.10a shows temperature distribution on the cross-section of the extracted wire with five different positions, from copper wheel contacted regions to the free surface. It is readily shown that the temperature near the wheel tip decreases dramatically in the first microsecond and decreases a little slower for the following time. The larger reduction of temperature near the wheel tip is responsible for the formation of concaves on the surface in Fig. 3.3a. The same changing tendency is also obtained for other cooling regions. Figure 3.10b shows the corresponding cooling rate distribution across the microwire. Excluding the larger drop of temperature in the instantaneous contact interval, the cooling experience of the whole extracted layer is herein divided into three stages, namely, (I) formation and moving within the puddle, (II) dwelling on the wheel tip, and (III) the separation from the wheel. In the first stage (before 3.6 ms), a thin liquid layer is accelerated in the puddle due to the combination of momentum and heat transfer by the extracted wheel. The cooling rate in this stage is very small, in that the whole layer moves within the puddle and the heat can transfer instantaneously from the remaining liquid to the thin accelerated layer. When the melt layer was extracted out of the puddle (3.6 ms, starting point of stage II), the temperature of the most part of the layer is above its crystallization temperature  $T_x$  (except for point 1, seen in Fig. 3.10a), indicating the extracted layer remains almost liquid after leaving the droplet. The layer dwells along the rotating direction and heat transfers from molten layer to the wheel tip. Thin amorphous layer solidifies along the wheel tip because of its high cooling rate (exceeding the order of  $10^6$  K/s), leading to the formation of shallow concave near the contact with the copper wheel. It should be noted that the temperature in this stage (3.6–5 ms) within the layer is still above its crystallization temperature, and the layer remains liquid after leaving the wheel, where surface tension acts as a dominant effect on the formation of circular microwire.

### 3.3 Mechanical Properties

#### 3.3.1 Tensile Property and Fracture Reliability

Quasi-static tensile tests were performed on an INSTRON 3343 micro-tensile testing setup with a load cell of 10 N at room temperature. The ASTM standard of D3379-75 with a regularly rectangle gauge length of 10 mm was chosen for preparing tensile samples. Uniaxial tensile tests were conducted at room temperature with a constant strain rate of  $4.2 \times 10^{-4} \text{ s}^{-1}$ . Figure 3.11a-c shows the tensile strength-strain curve and fracture morphology of Co-based extracted wires with diameters of about 60 and 40  $\mu\text{m}$ , respectively. The tensile strength of the thin uniform circular wire is approximately 3700 MPa, a little higher than the previous results, processed by glass-covered amorphous wires [45]. While for the wire with

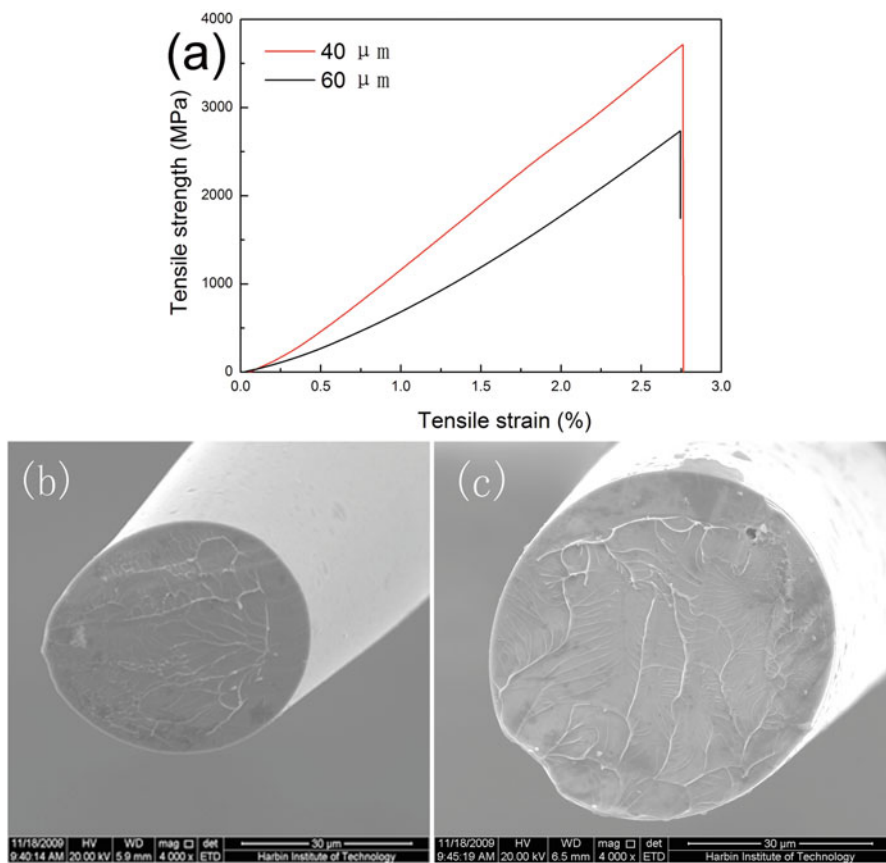


**Fig. 3.11** Tensile behavior (a) and fracture morphologies of Co-based wires with diameters of 40  $\mu\text{m}$  (b) and 60  $\mu\text{m}$  (c)

diameter of 60  $\mu\text{m}$ , its tensile property of approximately 2850 MPa is much lower than the previous one. The higher tensile strength can be explained by the low stress concentration, perfect geometry, and high amorphous nature. From Fig. 3.11b, c, it can be seen that both the fracture figures are composed of two regions: a relatively featureless zone produced by shear slip and a vein pattern produced by the rupture of the cross-section remaining after the initial shear displacement. However, the former wire of 40  $\mu\text{m}$  fractures along the maximum shear plane, which is declined by about 45 deg to the tensile direction, and some molten droplets form at the initial part of the vein pattern; for 60- $\mu\text{m}$  wires, tensile fracture occurs on a shear plane at 90° to the transverse section.

The strength data of brittle materials have been known to exhibit a wider degree of scatter compared to that of ductile materials, implying the reliability of structural applications. The statistical method commonly used to describe the distribution of fracture stresses in brittle materials is that given by Weibull [46]. The cumulative probability function of the Weibull distribution is expressed as follows:

$$P_f = 1 - \exp \left[ - \int_V \left( \frac{\sigma - \sigma_\mu}{\sigma_0} \right)^m dV \right] \quad (3.5)$$

where  $P_f$  is the probability of failure at a given uniaxial stress or lower, and can be calculated using the equation:  $P_i = \frac{i-0.3}{N+0.5}$ , where  $N$  is the total number of the samples tested and  $i$  is the sample ranking in ascending order of failure stress. The threshold value  $\sigma_\mu$  is the value below which no specimen is expected to fail. The term  $\sigma_0$  refers to a characteristic strength defined as the stress at which the  $P_f$  is 63.2%. The  $m$  is a parameter known as Weibull modulus, and  $V$  is the volume of the tested samples.

After rearranging, Eq. (3.1) can be written as

$$\ln \left\{ \ln \left[ \frac{1}{(1 - P_f)} \right] \right\} = m \ln(\sigma - \sigma_\mu) - m \ln \sigma_0 \quad (3.6)$$

When  $\sigma_\mu = 0$ , the distribution becomes the two-parameter Weibull distribution

$$\ln \left\{ \ln \left[ \frac{1}{(1 - P_f)} \right] \right\} = m \ln(\sigma) - m \ln \sigma_0 \quad (3.7)$$

Weibull modulus  $m$ , threshold value  $\sigma_\mu$  and characteristic strength  $\sigma_0$  thus can be obtained by fitting experimental data  $\left( \ln(\sigma_f), \ln \left\{ \ln \left[ \frac{1}{(1 - P_f)} \right] \right\} \right)$  with two-parameter and three-parameter method.

Eighteen samples were tested for these extracted microwires and displayed in Fig. 3.12. The apparent fracture strength  $\sigma_f$  ranges from 2843 to 3558 MPa, with a mean value of 3197 MPa and a variance of 235 MPa. The strength variation for these microwires results from the distribution of the strength-limiting flaws. For as-cast microwires, the flaws could stem from the concaves, casting pores,

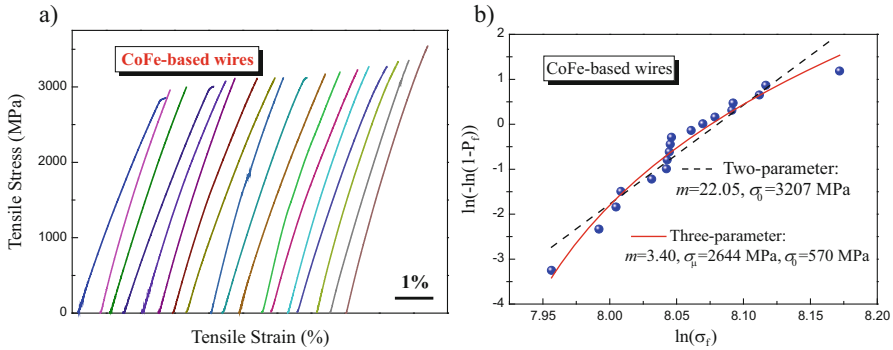


**Fig. 3.12** (a) Tensile stress–strain curves and (b) Weibull statistical analysis of Co-based microwires

inclusions or surface irregularities. Note that the existence of these flaws results in a severe deterioration of their mechanical properties, especially tensile strength and fracture reliabilities. Figure 3.12b shows the Weibull plots in the fashion suggested by Eqs. (3.6) and (3.7) for the extracted Co-based microwires. The data fits yield the following estimated parameters that describe the distributions:

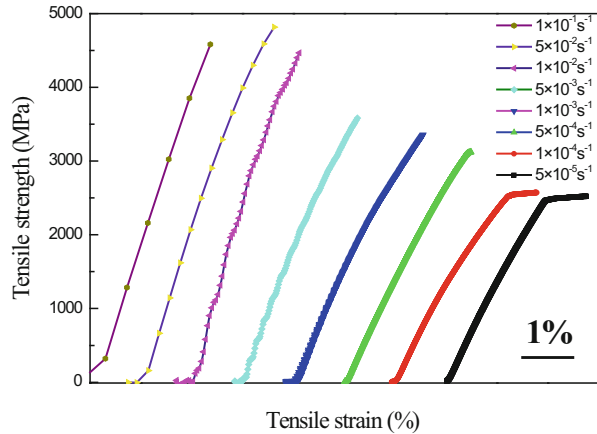
Two-parameter:  $m = 22.05$ ,  $\sigma_0 = 3207$  MPa

Three-parameter:  $m = 3.40$ ,  $\sigma_\mu = 2644$  MPa,  $\sigma_\sigma = 570$  MPa

### 3.3.2 Strain Rate Dependence

Understanding of the dynamic failure mechanism in microwires is important for the application of this class of materials to a variety of engineering problems. This is true for design environments in which components are subject to different loading rates. Typical tensile stress–strain curves of Co-based amorphous microwires on the range  $5 \times 10^{-5}$  to  $1 \times 10^{-1} \text{ s}^{-1}$  are shown in Fig. 3.13. The fracture stress increased gradually with increasing strain rate. The fracture stress increased from 2500 to 4500 MPa when the applied strain increased from  $5.0 \times 10^{-5}$  to  $1.0 \times 10^{-1} \text{ s}^{-1}$ , indicating a positive strain rate sensitivity. The stress–strain curves at  $5.0 \times 10^{-2}$  and  $1.0 \times 10^{-1} \text{ s}^{-1}$  exhibit linear slope till failure and no anelastic post-yielding were observed. With the decrease of strain rate, lower than  $5.0 \times 10^{-2} \text{ s}^{-1}$ , the stress–strain curve initially deforms elastically and further deviates from the linear deformation part, showing a nonlinear deformation behavior prior to fracture. With further reduction of the applied strain rate, the curves deformed at  $1.0 \times 10^{-4}$  and  $5.0 \times 10^{-5} \text{ s}^{-1}$  exhibit completely different shapes. After reaching the maximum stress, relatively large plastic flow with no strain hardening, typical of “ductile” failure, was observed in the tensile curves. Maximum tensile plasticity over 1% can be observed in this low strain range. Unlike most strain rate responses of bulk

**Fig. 3.13** Tensile stress–strain curves of Co-based amorphous microwires at different strain rates



metallic glasses, it is important to note that no serrated flow, mainly caused by the shear band initiation and propagation, was observed on the tensile curves over a wider strain range, indicating that the “ductile” failure behavior for the amorphous microwires at the low strain rate does not depend on the formation of new shear band.

Fractured specimens were examined to investigate the deformation behavior of microsized Co-based amorphous microwires. Figure 3.14a, c, e are the side views of the specimen fractured at the strain rate of  $5.0 \times 10^{-5}$ ,  $1.0 \times 10^{-4}$ , and  $5.0 \times 10^{-3} \text{ s}^{-1}$ , respectively. The whole three samples sheared off nearly at  $54^\circ$  to the tensile axis, essentially independent of strain rate in the present studies. The fracture characteristics of amorphous microwires yield the Mohr–Coulomb criterion rather than Von Mises rule. The side surface Fig. 3.14a, c, e appears to be smooth, no clear sign indicating the operation of other shear bands. The formation and propagation of one major shear band dominates the fracture of the sample, in accordance with previous observation as in Fig. 3.13. The fracture surface of the specimen at corresponding strain rate is shown in Fig. 3.14b, d, f. Smooth tearing deformation region, i.e. shear offset, and vein-like morphology is readily seen over the three specimens. The lengths of shear offset decrease with the applied strain rate while the density of vein-like pattern gives an opposite tendency.

The deformation and fracture behaviors of amorphous microwires are strongly dependent on the strain rate. The larger strain rate it imposed, the higher fracture strength it behaves. This result revealed in Co-based Pd<sub>40</sub>Ni<sub>40</sub>P<sub>20</sub> BMG in tension test. However, the tensile plasticity exhibits a contrary tendency. A possible explanation for the behavior as seen in Fig. 3.13 could be related to the creation, coalescence, and diffusion of free volume in these materials, whereas the creation and diffusion of free volume are influenced greatly by the applied strain rate. Spaepen et al. [48] developed a general constitutive equation to characterize the plastic deformation of amorphous alloys, which can be written as

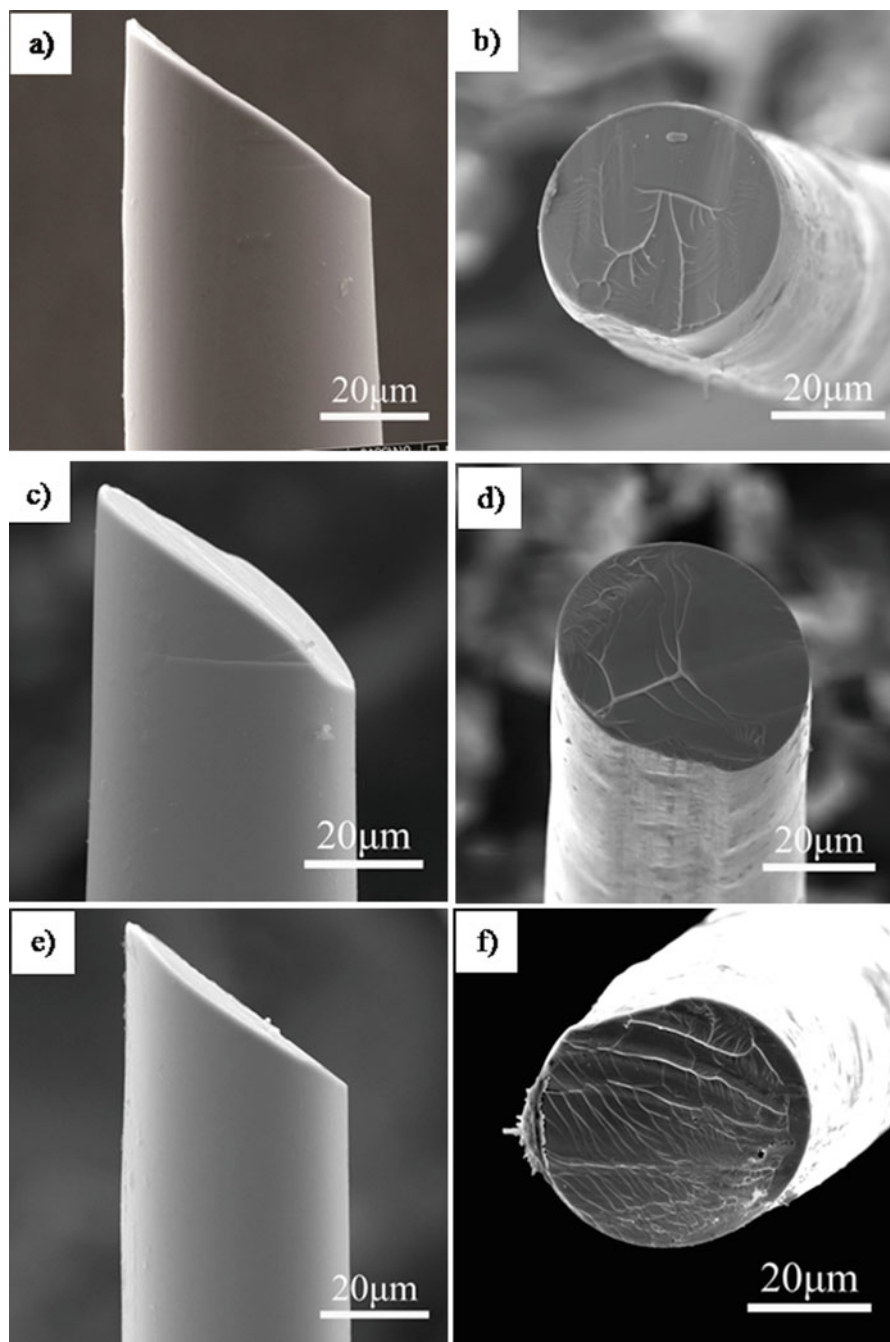


**Fig. 3.14** SEM images revealing fracture features of Co-based amorphous microwires with different strain rates (a), (b)  $5.0 \times 10^{-5} \text{ s}^{-1}$  (c), (d)  $1.0 \times 10^{-4} \text{ s}^{-1}$  (e), (f)  $5.0 \times 10^{-3} \text{ s}^{-1}$



$$\dot{\gamma} = \frac{\dot{\tau}}{\mu} + 2f \cdot \exp\left(-\frac{\alpha}{\xi}\right) \cdot \exp\left(-\frac{\Delta G}{k_B T}\right) \cdot \sinh\left(\frac{\tau \Omega}{2k_B T}\right) \quad (3.8)$$

where  $\dot{\gamma}$  is the shear strain rate,  $\dot{\tau}$  the applied shear stress,  $\xi$  the concentration of the free volume,  $\alpha$  a geometrical factor of order unity,  $f$  the frequency of atomic vibration,  $\Delta G$  the activation energy,  $\Omega$  the atomic volume,  $k_B$  the Boltzmann's constant,  $\mu$  the shear modulus, and  $T$  the absolute temperature. Apart from the thermodynamic and geometrical factor, the concentration of the free volume  $\xi$  also plays an important role in the deformation of amorphous alloys. The concentration of the free volume is the competition result between continuous creation by an applied shear stress and annihilation by structural relaxation due to atom rearrangement. The creation of free volume increases gradually with shear strain rate, while the free volume annihilation rate yields an opposite tendency. For those relatively high strain rates, the creation rate of free volume exceeds the annihilation rate, resulting in the decrease of viscosity or the increase of temperature on the shear plain and finally catastrophic failure. With the applied strain rate decreasing further, below  $1.0 \times 10^{-4} \text{s}^{-1}$ , the free volume annihilation rate exactly balances the stress-driven creation rate. As a result, the total net concentration of free volume remains constant, leading to a global tensile plasticity in Co-based amorphous microwires.

The absence of serrated flow and the existence of a pure slip region before final fracture in melt-extracted Co-based amorphous microwires indicate that the tensile fracture behavior of such small specimens over a wider strain range was dominated by the initiation and propagation of one major shear band. For the shear banding process of amorphous alloys, there exist two counteracting mechanisms: shear-induced accumulation of free volume within the shear band, leading to the stress drop in the stress-strain curve, and structure-induced annihilation, which can counteract the aforementioned softening effect. By analogy to the three structure evolution stages raised by Wu et al. [49] during deformation of bulk metallic glasses, we suggest that the whole tensile process of Co-based amorphous microwires can be divided into four stages: (1) elastic tensile deformation, (2) nonlinear tensile deformation, (3) stable propagation of shear band and uniform tensile plasticity, (4) final fast propagation and failure of shear band, as shown in Fig. 3.15. At the first stage, specimen deformed elastically with the applied stress and the density of the free volume increased gradually. In stage II, the excess free volumes agglomerate on the shear plane and shear band starts to form, sub-nanometer voids are coalesced from free volume at the same time due to the applied tensile stress. The formation of tiny voids probably consumes the applied strain energy and decreases the stress area thus gives rise to the nonlinear deformation behavior, which has been already confirmed in some small-sized metallic glasses. With shear deformation proceeding, in stage III for the low strain rate condition, the stress-driven creation rate of free volume is exactly balanced by the annihilation due to structure relaxation. Free volume has sufficient time to restructure and reconfigure to accommodate the applied strain rate. At the same time, the

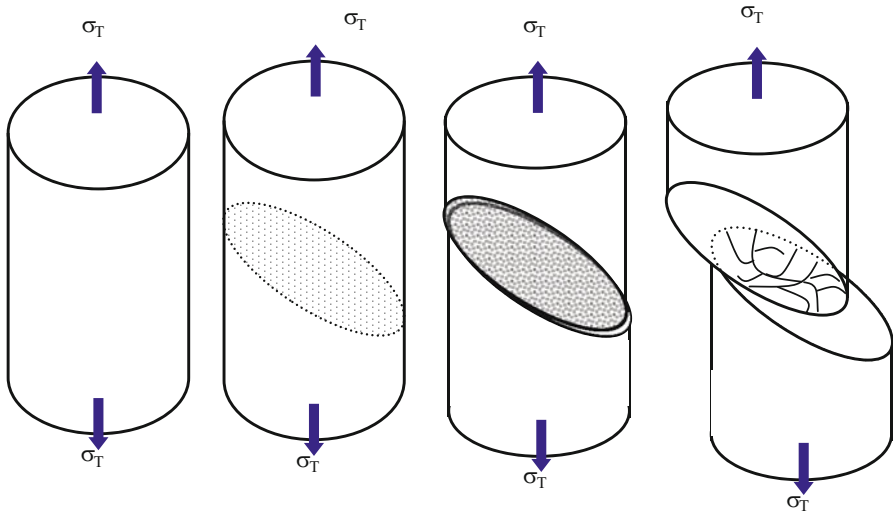


**Fig. 3.15** Schematic illustrations of tensile deformation and fracture process for Co-based amorphous microwire

voids agglomerated start to induce the formation of a local crack and slip steadily, resulting in the formation of shear offset on the fracture surface. The slow and stable propagation of shear crack yields a steady development of shear offset, leading to a global tensile plasticity in Co-based amorphous microwires. For the high strain rate condition, the balance between creation and annihilation of free volume will not occur. In the fourth stage, when the size of shear offset develops to a critical length, the shear band becomes unstable; any fluctuation of stress or free volume change will trigger the rapid propagation and final fast fracture of sample. The propagation behavior in these amorphous microwires is too fast to be observed experimentally. Vein patterns observed in Fig. 3.14b, d, f are the results of rapid propagation and fracture of shear band. The critical shear offset, i.e., the size of the smooth region on the fracture surface of amorphous samples after deformation, and tensile plasticity of amorphous microwires are strongly dependent on the imposed strain rate. The critical shear offset can be regarded as a parameter directly reflecting the stability of shear deformation. Therefore, it is suggested that the shear deformation capability of an amorphous microwire is related to its critical shear offset: the global plastic deformation of the amorphous microwire increases with increasing critical shear offset. For the Co-based amorphous microwires in the present work, decreasing strain rate will enlarge the critical shear offset and improve their plastic deformation dramatically.

### 3.3.3 Cold-Drawn Property

The continuous near-circular Co-based wires with diameter of about 60  $\mu\text{m}$  were fabricated by the melt extraction method. The diameter of the extracted wires was reduced step by step through a number of drawing processes using diamond dies without any intermitting annealing, as schematically shown in Fig. 3.16a [50]. The cross-section area reduction ratio,  $R = (D_0^2 - D_1^2)/D_0^2$ , where  $D_1$  is the diameter after drawing and  $D_0$  is the original diameter, was controlled within 4 % per step.

Co-based metallic wires were easily drawn to a cross-section area reduction of about 75 % without rupture. The outer surface of cold-drawn wire with different  $R$  values is shown in Fig. 3.16b. All of the drawing wires exhibit smooth surfaces without any visible scratches, while the grooves and fluctuations in the as-quenched wire, as indicated by the arrows, can be seen occasionally on the surface. Note that the existences of these flaws severely deteriorate their mechanical properties. After the drawing process, it can be seen that the grooves and flaws were removed; wires became more circular and round.

The effect of cold drawing on the mechanical performance of melt-extracted amorphous wires was investigated and the representative tensile stress–strain curves for microwires with different  $R$  values are presented in Fig. 3.17. The cold-drawn wires exhibit noticeable tensile plasticity as compared with the as-quenched sample (a). The tensile strain and tensile strength increase gradually with cross-section reduction until  $R = 51\%$  and then decrease with further deformation. Cold-drawn microwire with  $R = 51\%$  exhibits the highest tensile strength of 4320 MPa and a maximum tensile ductility of 1.09 %. It should be noted that curves (a), (b), and (c) possess similar elastic modulus, as calculated from the slope of these curves, while the modulus becomes slightly larger for samples (d), (e), and (f), indicating somewhat different structures of these two groups of wires.

To verify the wire's usefulness as a fine engineering material, it is necessary to evaluate its mechanical properties in the context of prevalent materials of same

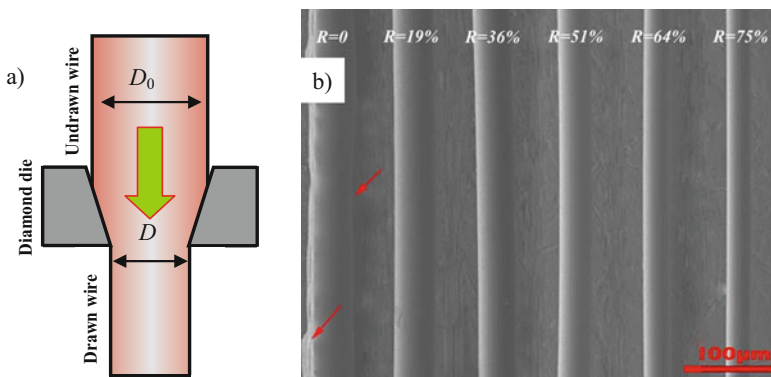
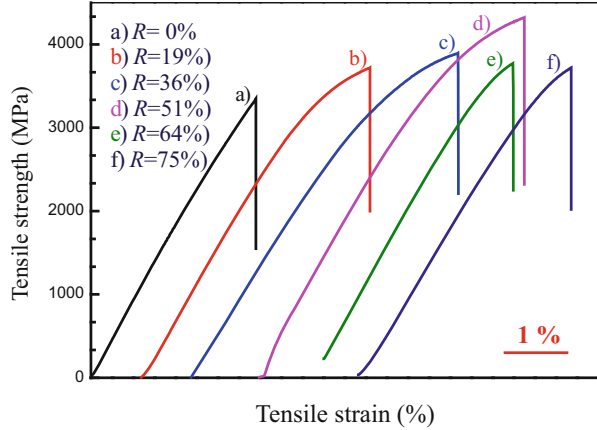


**Fig. 3.16** Principle of diamond cold drawing (a) and SEM images of melt-extracted wires with different cross-area reduction (b) [50]

**Fig. 3.17** Stress–strain curves for the metallic wires with different cross-section reductions



scale. The engineering stress–strain curve of the present 51 % cold-drawn wire together with a series of Zr-based [51, 52], Pd-based [53, 54], Fe-based [3], Mg-based [55], Ni-based [56, 57], and Co-based amorphous microwires [58] are compiled and presented in Fig. 3.18a. It can be clearly seen that, compared with other microwires fabricated by in-rotating-water quenching, glass coating and even conventional melt extraction methods, the present microwire exhibits the largest fracture absorption energy (fracture toughness), as characterized by the area underneath the stress–strain curves. Figure 3.18b compares the tensile stress versus tensile strain data for all of those above-mentioned wires and the microwire in the present study exhibits the highest tensile strength and the largest tensile ductility of all discussed samples.

Figure 3.19 presents X-ray diffraction patterns of the as-quenched and cold-drawn samples. Most of these samples exhibit consistent feature, i.e., a broad diffuse halo except for a small crystal peak overshadowed by the background noise for the 64 % drawn wires, indicating that cold drawing is an effective way to reduce the diameter of the melt-extracted microwire without changing its macro-scale structure constitute. This is especially important for the sensing application of wires, since they prefer to be thinned down to fine diameter in meeting the requirement of miniaturization but without compromising the mechanical integrity. It should be noted that the conventional XRD technique is unable to detect phases whose content is less than about 5 wt% (depending on crystal symmetry), the microscale structural change (if any) induced during cold-drawing process needs to be further clarified by electron microscopy.

Figure 3.20a–c gives the high-resolution transmission electron microscopy (HRTEM) images for the as-cast,  $R = 51\%$  and  $R = 64\%$  cold-drawn wires. No contrast and lattice fringe can be detected in Fig. 3.20a, demonstrating that the as-cast wire is fully amorphous without any nanocrystals. Compared with the as-cast structure, isolated nanocrystallites with an average size of 4 nm distributed homogeneously in the amorphous matrix were observed for the  $R = 51\%$  sample (Fig. 3.20b). The degree of nanocrystallization becomes higher and more obvious

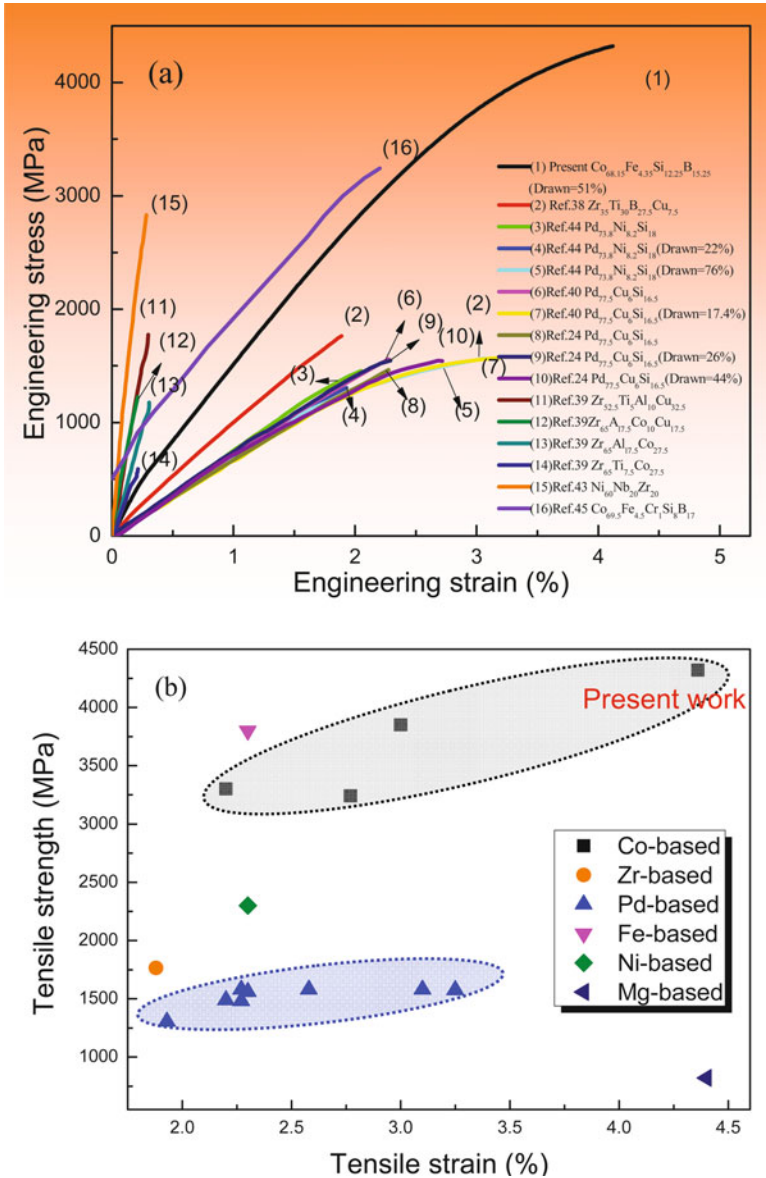


**Fig. 3.18** (a) Tensile stress–strain curves for a series of amorphous microwires; (b) Tensile strength plotted against the tensile ductility at room temperature

for the  $R = 64\%$  wire as seen in Fig. 3.20c. These inhomogeneities embedded in the amorphous matrix are believed to arrest the fast extension of shear band and stabilize the sample against the catastrophic failure, resulting in the enhanced ductility.

**Fig. 3.19** X-ray diffraction patterns of the as-quenched and cold-drawn microwires

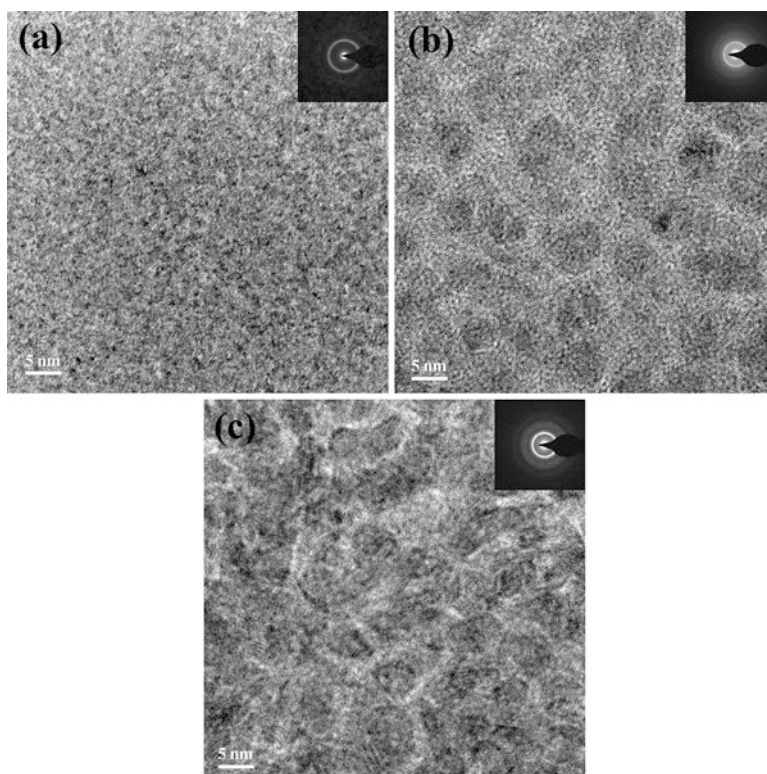
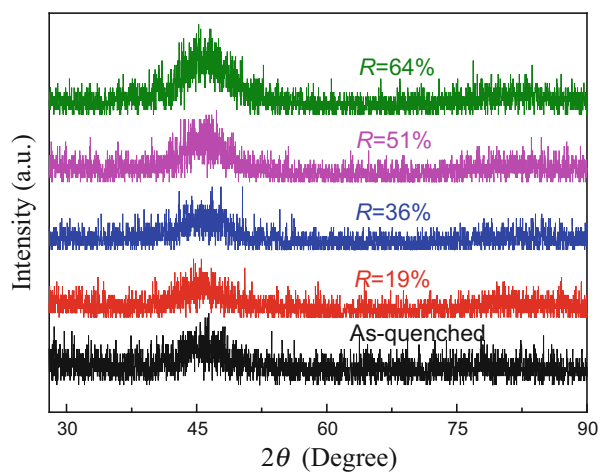


**Fig. 3.20** High-resolution transmission electron microscope patterns of the different cold-drawn extracted microwires (a) as-quenched, (b) 51% and (c) 75% cold-drawn microwires

In another perspective, residual stress generated in the drawing process can also affect their mechanical properties. The axial residual stress  $\sigma_x$  and circumferential residual stress  $\sigma_n$  can be given by:

$$\sigma_x = \frac{B}{B-1} \sigma_y \left[ 1 - \left( \frac{D}{D_0} \right)^{2(B-1)} \right], \quad (3.9)$$

$$\sigma_n = \frac{B}{B-1} \sigma_y \left[ \left( \frac{D}{D_0} \right)^{2(B-1)} - \frac{1}{B} \right], \quad (3.10)$$

where  $B$  is constant and related to the geometry of die,  $\sigma_y$  is the yield strength of the sample,  $D$  and  $D_0$  represent the diameter at position  $x$  and initial diameter.

Because of its low deformability, the area reduction ratio of Co-based metallic wires was limited to 4% per each step, thus the stress of the wires when extracted out of the diamond die can be calculated as:  $\sigma_x = 0.115\sigma_y$ ,  $\sigma_n = 0.885\sigma_y$ , respectively. Bear in mind that the compressive surface residual stress is beneficial for the increase of hardness and fracture strength, while the tensile residual stress has the opposite effect [25, 48–50]. Thus  $\sigma_n \gg \sigma_x$ , suggesting that the circumferential compressive stress benefits the mechanical performance of the drawn wires.

## 3.4 Magnetic Behavior

### 3.4.1 Giant Magnetoimpedance

Giant magnetoimpedance refers to a significant change of ac impedance occurred to a soft magnetic material carrying a driving ac current when it is submitted to a dc magnetic field [5]. This effect has aroused much research interest due to its promising applications in various sensing devices. Among other GMI materials, microwires are recognized most privileged sensing element with extraordinary GMI effect for high-performance sensing applications [59]. Therefore, much research efforts have been devoted to modulation and optimization of the microwires' microstructure and domain structure for better GMI effect.

The giant magnetoimpedance (GMI) effects of the microwires fabricated at different cooling speeds mentioned above were systematically studied and Fig. 3.21 exhibits their GMI results measured at different frequencies: 0.1, 0.5, 1, 5, 10, and 15 MHz. The GMI ratios ( $\Delta Z/Z_{\max}(\%)$ ) of Co-based microwires fabricated by Cu wheel at 5 m/s and 30 m/s are 27% and 8.1% at 0.1 MHz, respectively, and 97% and 78.6% at 0.5 MHz, respectively. The GMI ratios increase with the Cu wheel speeds (>1 MHz) and the maximum GMI ratio at 30 m/s reaches 360% at 10 MHz, then the value declined slightly at 15 MHz. The Mo wheel has relatively lower thermal conductivity compared with Cu wheel thus resulting in the difference in microstructures. The GMI ratio for microwires

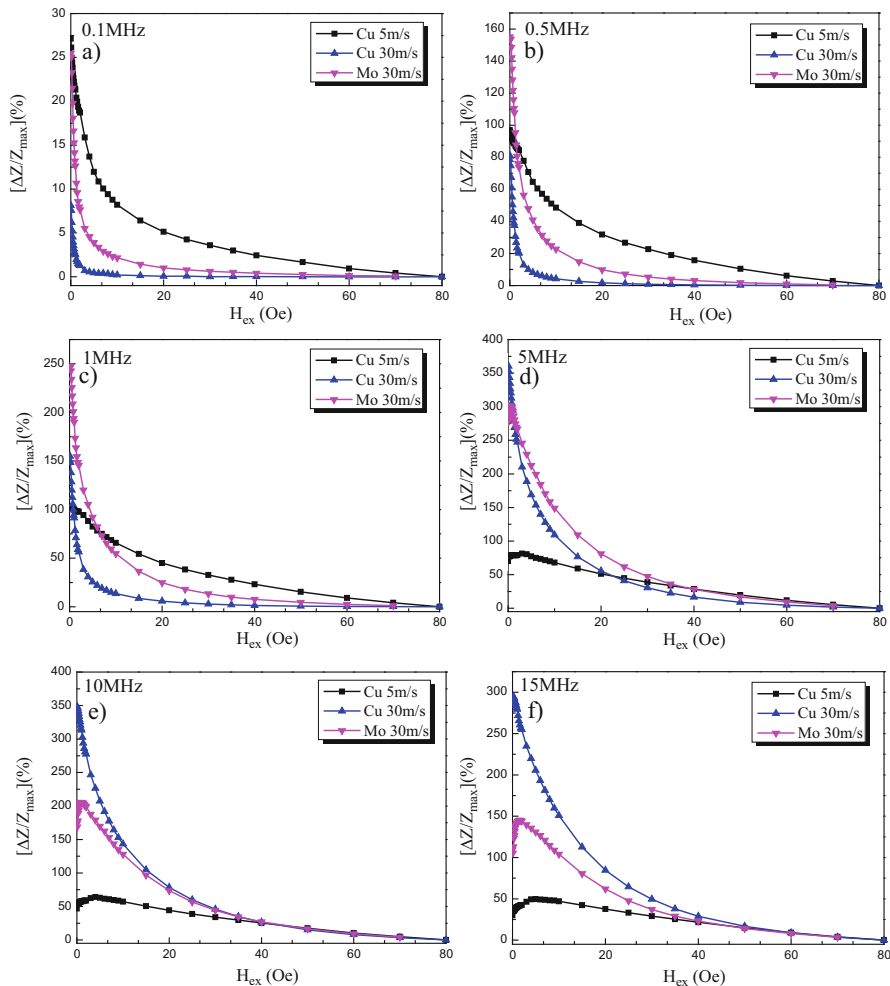


**Fig. 3.21** Magnetic field dependence of GMI ratio  $\Delta Z/Z_{\max}$  at different frequencies for the different extracted microwires (a)  $f=0.1$  MHz; (b)  $f=0.5$  MHz; (c)  $f=1$  MHz; (d)  $f=5$  MHz; (e)  $f=10$  MHz; (f)  $f=15$  MHz

obtained under Mo 30 m/s is larger than that of Cu 30 m/s microwires when measured frequencies is lower than 1 MHz but the GMI ratio becomes lower when the applied frequencies larger than 5 MHz. It has been reported that the GMI curves show typical symmetry under the applied positive and negative magnetic fields with single peaks and double peaks behaviors. The GMI ratios of Cu 30 m/s microwires exhibit monotonically decreasing with the increase of applied



field for all measured frequencies, while the GMI curves of Mo 30 m/s and Cu 5 m/s microwires show double peaks behavior for frequencies larger than 5 MHz and their equivalent magnetic anisotropy fields increased to larger than 2 Oe.

Commonly, the GMI effects of melt-extracted microwires show high dependence on their compositions, measurements, distribution of residual stresses, and microstructures. The residual stresses in the microwires increased with the solidification rate which related to the revolving speed of wheel, moreover the stress distribution on the surface of the wires is nonuniform due to the unilateral heat transfer during the melt-extracted process thus result in the change of stress anisotropy. The large residual stresses lead to large magnetoelastic energy which results in the difficulties in magnetic domain switching or moving, so the microwires fabricated at high wheel speed exhibit relatively hard magnetization and small GMI ratios at low applied fields. The magnetocrystalline anisotropy of Mo 30 m/s microwires and Cu 5 m/s microwires increases due to the hard magnet phases  $\text{Fe}_3\text{Si}$ ,  $\text{Co}_2\text{B}$ , and  $\text{Co}_2\text{Si}$  which obstruct magnetic domain switching or moving as pinning points, then reduces both the magnetic conductivity and GMI effect, thus the GMI curves show typical double peak behaviors.

The dependence of the GMI ratios at 10 and 15 MHz as a function of applied axial magnetic field  $H$ , for different  $R$  values, i.e., as-cast, 19, 36, 51, 64 %, is presented in Fig. 3.22. One can see that, at both frequencies, all the wires including the as-cast wire show double-peak features. The shape of curves and the amplitude of GMI ratio ( $\Delta Z/Z$ ) as well as the anisotropy field ( $H_k$ ) at which the maximum GMI ratio occurs depend intimately on the cross-section area reduction. To clearly elucidate the role of each drawing step on the GMI characteristics of microwires, we plotted the field dependence of maximum GMI ratio ( $(\Delta Z/Z)_{\max}$ ) and anisotropy field ( $H_k$ ). The  $(\Delta Z/Z)_{\max}$  decreased dramatically after the initial drawing process, for example, from 134 % to 88 % at 10 MHz for  $R = 19$  %. With further deformation, the  $(\Delta Z/Z)_{\max}$  starts to increase and reaches a maximum of 160 % at 7 Oe for  $R = 51$  % before decreases again with increasing  $R$  up to 64 %. The anisotropy field ( $H_k$ ) undergoes a rapid increase from 1 Oe to 5 Oe at 10 MHz after the first drawing step before a relatively small increase of 2 Oe with further drawing. Afterwards the anisotropy field levels off at 7 Oe. Overall the simple cold-drawing process proves to be capable of enhancing the GMI ratio by 30 % and the anisotropy field by a factor of 7 in comparison with those of as-cast wire, respectively. The effect of each cold-drawing step remains the same trend at both frequencies. Yet it should be noted that at 15 MHz the maximum improvement of GMI ratio is 44 %, much larger than 26 % at 10 MHz, whereas the maximum increase of anisotropy field is quite similar, i.e., 6 and 6.6 Oe, respectively. Such a simultaneous large improvement of maximum GMI ratio and anisotropy field is particularly important for the magnetic sensing application which requires a strong response and a wide measurement range.

Compared with the as-cast microwire, melt-extracted microwires after cold drawing exhibit a higher GMI ratio except for an initial drop for the  $R = 19$  % sample. The distribution of stress generated in the quenching process and the added external stress throughout the wire volume as well as the microstructural evolution

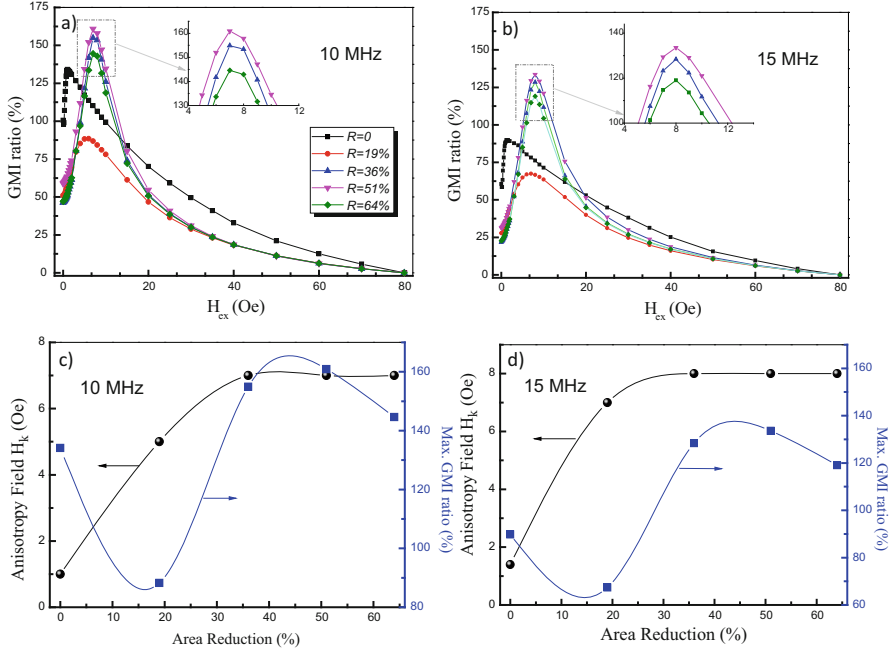


**Fig. 3.22** Field dependence of the GMI ratio  $\Delta Z/Z$  and maximum GMI ratio and anisotropy field at different frequencies for the as-quenched and cold-drawn wires (a), (c) 10 MHz; (b), (d) 15 MHz

during drawing process play decisive roles in the determination of its magnetization configuration, and hence its magnetic performance. In this section, we discuss the effect of the longitudinal tensile stress and circumferential compressive residual stress generated during drawing process and the size of those mechanical-induced nanocrystals on the evolution of magnetic domain configuration. The magnetic anisotropy of amorphous wires is mainly determined by magnetoelastic interactions due to the absence of magnetocrystalline anisotropy (for  $R < 51\%$ ) and negligible shape anisotropy. The magnetoelastic energy density of an amorphous can be formulated as [60]:

$$w_{m-el} = -\frac{3}{2}\lambda_s \left( \sigma_{rr}^{(q)} \alpha_r^2 + \sigma_{\varphi\varphi}^{(q)} \alpha_\varphi^2 + \sigma_{zz}^{(q)} \alpha_z^2 \right), \quad (3.11)$$

where  $\lambda_s$  is the saturation magnetostriction constant,  $\sigma_{ii}^{(q)}$  are the diagonal components of the residual stress tensor in cylindrical coordinates ( $r, \varphi, z$ ); and  $\alpha_i$  are the components of the unit magnetization vector. The residual quenching stress throughout the wire is assumed to be a function of reduced wire radius  $x$  ( $r/r_0$ ), and can be reasonably approximated by means of the following simplified relations [55]:

$$\sigma_{rr}^{(q)}/\sigma_y = a(1 - x^2), \quad (3.12)$$

$$\sigma_{\varphi\varphi}^{(q)}/\sigma_y = a(1 - 3x^2), \quad (3.13)$$

$$\sigma_{zz}^{(q)}/\sigma_y = b(1 - 2x^2), \quad (3.14)$$

where  $a$  and  $b$  are the constants relevant to the material property.

Figure 3.23a illustrates such radial dependence of residual stress. There exists an intersection at  $x_1$  for  $\sigma_{\varphi\varphi}^{(q)}/\sigma_y$  and  $\sigma_{zz}^{(q)}/\sigma_y$ . The inner core and out shell is then classified at this point for an as-prepared amorphous wire with negative magnetostriction, and  $x_1$  is the inner core radius, where the easy axis is along the wire due to  $\sigma_{zz}^{(q)}/\sigma_y < \sigma_{\varphi\varphi}^{(q)}/\sigma_y$ ; for outer surface ( $r > x_1$ ),  $\sigma_{zz}^{(q)}/\sigma_y > \sigma_{\varphi\varphi}^{(q)}/\sigma_y$  results in a circumferential anisotropy. The corresponding core-shell domain structure for the as-cast wire is shown in Fig. 3.23b, consisting of the outer shell circular domains and inner core axial domains. While for the cold-drawn wires, the existence of circumferential compressive stress and longitudinal tensile stress will cause a change in the volume fraction of outer shell circular domains and inner core axial domains, i.e., the outer shell domains become larger and the inner core domains are reduced accordingly, as depicted in Fig. 3.23c, but the domain configuration remains unchanged. This can be mathematically interpreted as the movement of intersection  $x_1$  for the  $\sigma_{\varphi\varphi}^{(q)}/\sigma_y$  and  $\sigma_{zz}^{(q)}/\sigma_y$ . As demonstrated in a previous study [61], a larger GMI

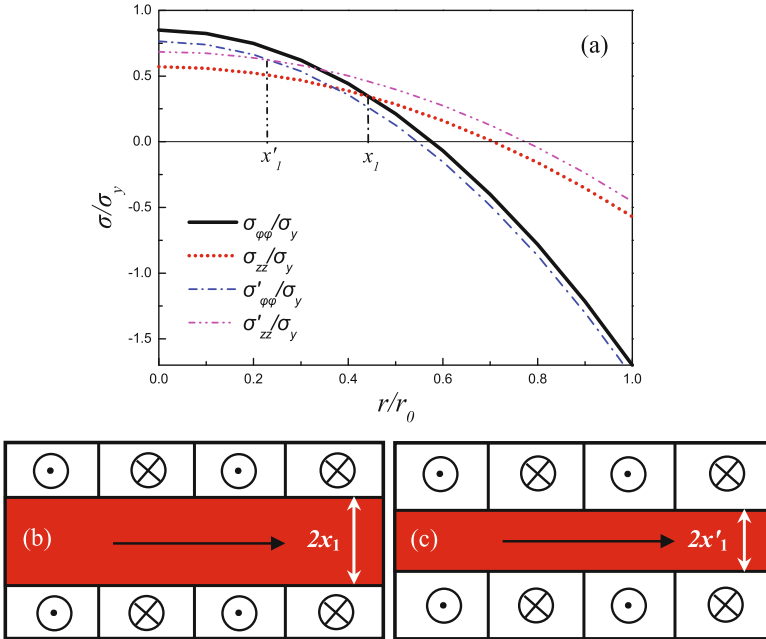


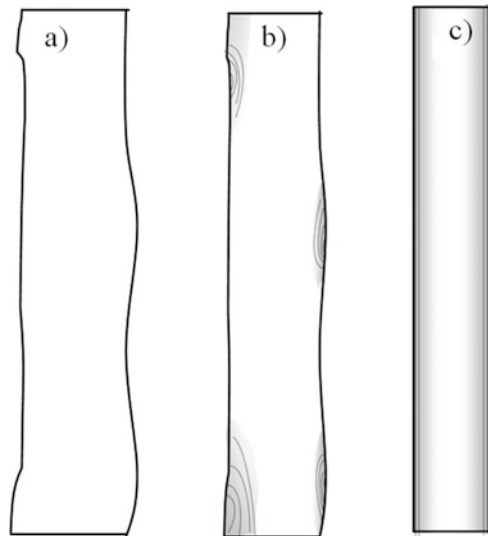
**Fig. 3.23** (a) Radial dependencies of residual stress tensor components in Co-base microwire and the corresponding domain structure for the (b) as-quenched and (c) cold-drawn samples

effect in Co-rich amorphous wire was achieved by an external axial tensile stress due to the rearrangement of the domain wall induced by tensile stress and the increase in circular anisotropy and permeability. The coupling effect of external axial tensile stress and residual quenched axial stress  $\sigma_{zz}$  will cause the intersection  $x_1$  move to the left, increasing the outer shell circular domains. In analogy, the circumferential compressive residual stress will cause a smaller  $\sigma_{\varphi\varphi}$ , similarly result in the intersection moving slightly to the left, i.e. point  $x'_1$ . As such, the axial residual tensile stress and circumferential compressive stress induced by cold-drawing process together increase the volume of outer shell and hence the circumferential permeability, giving rise to an improved GMI ratio.

Based on the above analyses, one would expect a monolithic increase of GMI ratio with further drawing process, however, Fig. 3.22 shows a complex field dependence of maximum GMI ratio. Thus the residual stress can only explain the increase of GMI from  $R = 19$  to 51 %. To understand the large reduction of GMI for the initial drawing steps, one need to consider the imperfect geometries of wires, which are expected to act as defects to cause stress concentration at the surface during the cold-drawing process, as schematically shown in Fig. 3.24. Along with the SEM images in Fig. 3.16b, it can be seen that the inhomogeneous surface of as-cast wire is forced into several stress-concentrated local regions, which will result in the inhomogeneities of magnetoanisotropy energy in the surface and deteriorate the soft magnetic properties. As exactly a surface related property, GMI effect is reduced sharply.

In another perspective, as discussed above, mechanical-induced nano-scale crystals formed during the cold-drawing process have a significant effect on the GMI properties. Isolated small-sized nanocrystals of less than 4 nm embedded in the amorphous matrix for the 51 % drawn sample yields a maximum GMI ratio of

**Fig. 3.24** Schematic illustration of the residual stress distribution in the microwires with different deformation degree (a) as-cast; (b)  $R = 19\%$ ; (c)  $R = 51\%$



about 160 % at 10 MHz. This phenomenon can be attributed to the residual stress generated during the drawing process, as the effect of crystalline anisotropy is negligible in this case. When the deformation is beyond the observed critical point of  $R = 51$  %, we can see from Fig. 3.20c that the size of these Co-rich nanocrystals become larger, with diameter exceeding 10 nm, and these crystals become nearly touched with each other. The existence of these nanocrystals with large size causes an increase of magnetocrystalline anisotropy and the magnetic hardness, deteriorating the soft magnetic property and hence the reduction of GMI ratio.

The last point deals with the effect of deformation on the anisotropy field which is governed by the magnetostriction constant  $\lambda_s$ , saturation magnetization  $M_s$  and the difference between  $\sigma_{zz}$  and  $\sigma_{\phi\phi}$  and can be expressed as [62]:

$$H_k = \frac{3\lambda_s}{M_s} (\sigma_{zz} - \sigma_{\phi\phi}) \quad (3.15)$$

As the difference between  $\sigma_{zz}$  and  $\sigma_{\phi\phi}$  increases with cold-drawing process as shown in Fig. 3.10, the anisotropy field then increases accordingly. However, instead of a linear increase with increasing reduction area, the anisotropy field became constant after  $R = 36$  %. In a reverse way of reasoning, this suggests the difference between  $\sigma_{zz}$  and  $\sigma_{\phi\phi}$  could become smaller. Indeed, as shown in a previous study [63], the circumferential stress exhibits a peak feature with increasing reduction area, i.e., the stress increases first and then decreases. This explains the observed evolution of anisotropy field with the wire area reduction. It is desirable to conduct a similar quantitative analysis for the present wires, which will be addressed in future work.

### 3.4.2 Magnetocaloric Property

Magnetic cooling technique has drawn much attention since it involves no environmental hazardous gas that is essential for conventional gas-compression technique. The cooling technique is realized through the adiabatic temperature change or the isothermal entropy change in response to an applied magnetic field in a material, i.e. magnetocaloric effect [64]. In comparison with the gas-compression cycle, the magnetic cooling cycle has much higher efficiency [65]. Therefore, significant research efforts have been devoted to exploring new MCE materials and devices. As compared to other form of MCE materials, microwires have the following advantages [46, 66]: (1) large surface area to volume ratio, which ensures a high cooling efficiency. (2) large aspect ratio, which means small demagnetization factor; (3) wire bundles have large operation frequency and favor a high-performance active magnetic refrigeration system.

Obviously, compared with bulk metallic glass (BMG), a strongly shape anisotropy appears due to the unique shape of the microwires and which may resulting in the anisotropy of magnetic properties. In order to investigating the influence of

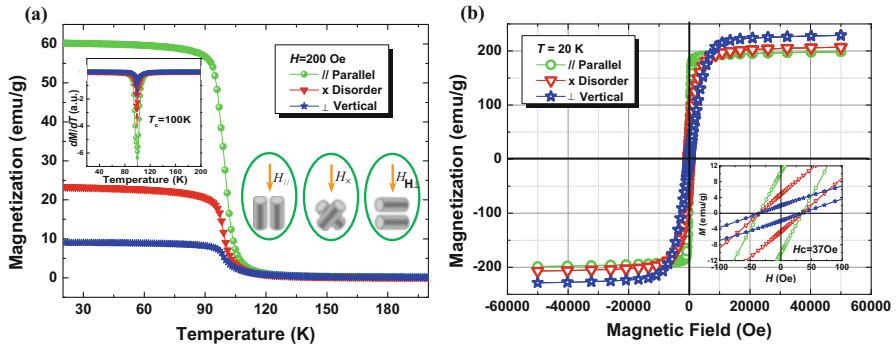


**Fig. 3.25** (a) Temperature dependences of FC magnetization taken at a field of 200 Oe for three different microwire arrangements, *insets* are the plot of  $dM/dT$  vs.  $T$  (*left hand*) and schematic diagrams (*right hand*) of three different microwire arrangements. (b) Magnetic hysteresis loops ( $M$ - $H$ ) for three microwire samples with different arrangements taken at 20 K, the *inset* shows the  $M$ - $H$  loops at low applied magnetic field

microwire shape anisotropy, three different microwire arrangements were designed and performed: the microwires were arranged parallel ( $//$ ), disorder ( $\times$ ), and vertical ( $\perp$ ) versus the direction of applied field, respectively, as schematically shown in inset (right hand) of Fig. 3.25a. The temperature dependence field-cooled (FC) taken at 200 Oe of three different arrangements was displayed in Fig. 3.25. Therefore, it can be observed that the microwires undergo a paramagnetic to ferromagnetic (PM-FM) transition. The Curie temperature  $T_C$ , defined by the minimum in  $dM/dT$ , is determined to be about 100 K, as plotted and shown in inset (left hand) of Fig. 3.25a. It is noticeable that the magnetization is much larger and the PM-FM transition is broader for the axis of microwires ( $//$ ) arranging parallel to the applied field. Figure 3.25b displays the magnetic hysteresis loops ( $M$ - $H$ ) taken at 20 K of different microwires arrangements. As coupled with inset in the Fig. 3.25b, micromicrowires exhibit a soft ferromagnetic characteristic ( $H_C \sim 37$  Oe), which is desirable for magnetic refrigeration applications. The square shape of the  $M$ - $H$  loop ( $//$ ) indicates that the easy magnetization direction is parallel to the micromicrowire axis. Remarkably, the  $M$ - $H$  loop ( $\perp$ ) of microwire axis arranging vertical to test field displays the largest saturation magnetization in large applied field ( $M_s = 229$  emu/g,  $\Delta H = 5$  T),  $\sim 15\%$  larger than that of parallel to the applied field ( $M_s = 199$  emu/g,  $\Delta H = 5$  T).

Figure 3.26a–c shows the isothermal magnetizations ( $M$ - $H$ ) curves for the three microwire arrangements in the applied field. The results for all above cases are displayed in Fig. 3.26a–c. Further to explore the nature of the magnetic phase transitions in the present samples, Arrott plots have been constructed based on the  $M$ - $H$  data (Fig. 3.26d–f). As displayed, the sign of the slope of  $M^2$  vs  $H/M$  is determined by the nature of a PM to FM transition, and the positive slope corresponding to a second order transition for all the microwire samples. Notably, due to the shape anisotropy of the microwires, the magnetizations of all

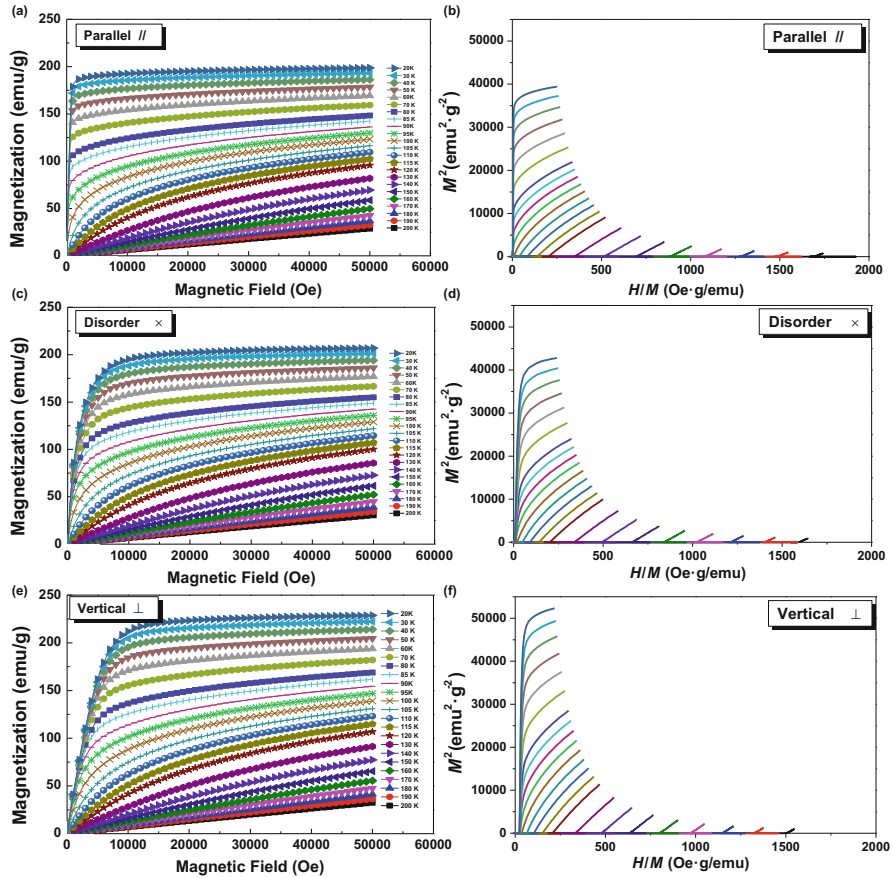
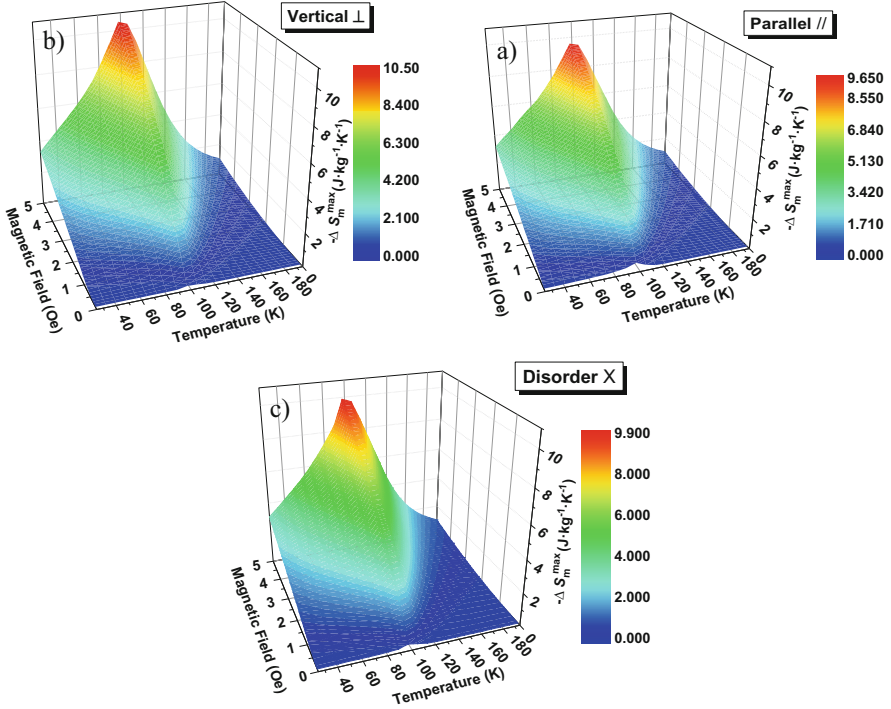


Fig. 3.26 Isothermal magnetization curves at different fixed temperatures between 20 and 200 K

temperatures can easily reach its saturation state at low magnetic fields for the case (//) of microwire sample parallel arrangement compared with the other two cases (× or ⊥). The obtained exciting results indicated that a larger isothermal magnetic entropy change ( $-\Delta S_m$ ) can be induced by a low magnetic fields for the // sample. Just this characteristic is favorable for practical applications of magnetic refrigerators, i.e. more economical permanent magnets can be provided as a magnetic field source instead of using expensive superconducting magnets.

The magnetic entropy change ( $-\Delta S_m$ ) of the samples has been calculated from the  $M-H$  isotherms by integrating throughout the whole magnetic fields:



**Fig. 3.27** Temperature dependence of magnetic entropy change ( $-\Delta S_m$ ) for different field changes up to 5 T (a) for the “//” sample, (b) for the “⊥” sample and (c) for the “X” sample

$$\Delta S_m(T, H) = S(T, H) - S(T, 0) = \int_0^{H_{\max}} \left( \frac{\partial M}{\partial T} \right)_H dH \quad (3.16)$$

where  $H$  represents the magnetic field,  $M$  denotes the magnetization, and  $T$  is the temperature. Then the results of  $-\Delta S_m$  vs.  $T$  under different magnetic fields for the three microwire samples are plotted in Fig. 3.27a–c. As desired, all microwire samples with different arrangement all display large values of magnetic entropy change ( $-\Delta S_m$ ) around the  $T_C$  and broad magnetic entropy change peaks. Remarkably, a larger peak value of isothermal magnetic entropy change ( $-\Delta S_m^{\max}$ ) and broader  $-\Delta S_m$  vs.  $T$  curves were achieved at a low magnetic fields ( $< 2$  T) for the // sample compared with the other two cases. Mostly interested, the  $\perp$  sample shows a superior peak value of magnetic entropy change ( $-\Delta S_m^{\max}$ ,  $\sim 10.6 \text{ J} \cdot \text{Kg}^{-1} \cdot \text{K}^{-1}$ ) at 5 T) than the other sample at large applied magnetic field ( $> 2$  T).



### 3.5 Conclusions

The melt extraction technique can be fruitfully employed to fabricate amorphous, nanocrystalline, and dual-phase amorphous/nano-crystal metallic wires by controlling process parameters during fabrication process and post treatment like annealing and drawing. These microwires exhibited excellent mechanical and magnetic properties, which depend both on the composition design, process optimization and post treatments. The following conclusions can be drawn from previous works:

- (a) Wire extraction mainly resulted in three geometries: uniform wires with concaved track at extracted wheel speed 5 m/s, wires exhibiting Rayleigh waves between 5 and 30 m/s, uniform wires with circular cross-sections at higher wheel speed 30 m/s. The formation of wavy wires is due to the Rayleigh instabilities and surface tension effect which tend to reduce the free surface area of the extracted liquid layer.
- (b) Wetting is a key parameter in the melt extraction process. Wetting behavior during melt extraction is distinct and different from conventional sessile drop method and dynamic wetting behavior. Besides the existence of shear force acting at the contact between the wheel tip and molten, supercooling or solidification occurs during the extraction process and, therefore, extraction could be processed.
- (c) Analysis of the controlling mechanism in the melt extraction process shows that, both thermal and viscous, i.e., momentum transport mechanism, are involved in the different process conditions. The controlled mechanism in the optimum process region is momentum transport.
- (d) The extracted amorphous microwires exhibit high mechanical properties and fracture reliability. The fracture strength of Co-based microwires with diameter of 40  $\mu\text{m}$  is approximately 3700 MPa. The Weibull modulus is 22.05 for the two-parameter Weibull static calculation, and the threshold value can be reached as high as 2644 MPa for the three-parameter Weibull static calculation.
- (e) The fracture strength of the Co-based amorphous microwire gradually increased with the strain rates, while the tensile plasticity increased with decreasing strain rate. At strain rates below  $1.0 \times 10^{-4} \text{ s}^{-1}$ , due to the balance of creation and annihilation of free volume, large dimensions of shear offset were formed on the fracture surface, leading to a pronounced tensile plasticity in Co-based amorphous microwires.
- (f) The Co-based microwires can be successfully cold drawn with up to 75 % cross-section area reduction. Tensile ductility, tensile strength as well as the GMI effect of the drawn wires increased with cold drawing and reached a peak of 1.09 %, 4320 MPa and 160 %, respectively, at 51 % cross-section area reduction and followed by a reduction with further deformation.
- (g) Nano-sized crystallites precipitated during drawing can stabilize the shear bands and arrest its fast propagation, leading to an enhanced ductility. The residual stress not only accelerates the amorphous-to-nanocrystalline phase

transformation but also contributes to the mechanical and magnetic properties. Both GMI ratio and anisotropy field are significantly improved after cold drawing.

- (h) Amorphous Gd-based microwires show excellent magnetocaloric properties due to the short-range order structure and size effect. The design and fabrication of a magnetic bed made of these multiple single parallel-arranged microwires would be a very promising approach for active magnetic refrigeration for nitrogen liquefaction.

The simultaneous achievement of high mechanical and magnetic properties opens up abundant possibilities of producing a variety of magnetic, stress and biological sensors or microwires enabled multifunctional composites.

**Acknowledgement** The authors gratefully acknowledge the financial support from the Natural Science Foundation of China (NSFC 51371067, 51671171 and 51501162) and Zhejiang Provincial Natural Science Foundation of China (LY16E010001). HW also acknowledges useful discussions with Hongxian Shen, Jingshun Liu, Shuling Zhang, and Lunyong Zhang from the Harbin Institute of Technology, PR China.

## References

1. Strom-Olsen, J.: Fine wires by melt extraction. *Mater. Sci. Eng. A Struct. Mater. Prop. Microstruct. Process.* **178**, 239–243 (1994)
2. Vazquez, M., Hernando, A.: A soft magnetic wire for sensor applications. *J. Phys. D Appl. Phys.* **29**, 939–949 (1996)
3. Waseda, Y., Ueno, S., Hagiwara, M., Aust, K.: Formation and mechanical properties of Fe- and Co-base amorphous alloy wires produced by in-rotating-water spinning method. *Prog. Mater. Sci.* **34**, 149–260 (1990)
4. Chiriac, H., Ovari, T.A.: Amorphous glass-covered magnetic wires: preparation, properties, applications. *Prog. Mater. Sci.* **40**, 333–407 (1996)
5. Phan, M.-H., Peng, H.X.: Giant magnetoimpedance materials: fundamentals and applications. *Prog. Mater. Sci.* **53**, 323–420 (2008)
6. Qin, F.X., Peng, H.-X.: Ferromagnetic microwires enabled multifunctional composite materials. *Prog. Mater. Sci.* **58**, 183–259 (2013)
7. Donald, I.W., Metcalfe, B.L.: Preparation, properties and applications of some glass-coated metal filaments prepared by the Taylor-wire process. *J. Mater. Sci.* **31**, 1139–1149 (1996)
8. Zhukov, A., Zhukova, V., Blanco, J.M., Gonzalez, J.: Recent research on magnetic properties of glass-coated microwires. *J. Magn. Magn. Mater.* **294**, 182–192 (2005)
9. Ochin, P.: Shape memory thin round wires produced by the in rotating water melt-spinning technique. *Acta Mater.* **54**, 1877–1885 (2006)
10. Yamasaki, J., et al.: Magnetic properties of Co-Si-B amorphous wires prepared by quenching in-rotating water technique. *IEEE Trans. J. Magn Jpn.* **4**, 360–367 (1989)
11. Chiriac, H., Ovari, T.A., Vazquez, M., Hernando, A.: Magnetic hysteresis in glass-covered and water-quenched amorphous wires. *J. Magn. Magn. Mater.* **177–181**, 205–206 (1998)
12. Hagiwara, M., Inoue, A., Masumoto, T.: Mechanical properties of Fe-Si-B amorphous wires produced by in-rotating-water spinning method. *Metall. Mater. Trans. A* **13**, 373–382 (1982)
13. Maringer, R.E., Mobley, C.E.: Advances in melt extraction. *Rapid Quenched Metals III.* **446**, 49–56 (1978)

14. Wang, H., Xing, D., Wang, X., Sun, J.: Fabrication and characterization of melt-extracted Co-based amorphous wires. *Metall. Mater. Trans. A* **42A**, 1103–1108 (2010)
15. Allahverdi, M., Drew, R.: *Melt Extraction of Oxide Ceramic Wires*. Montreal, McGill University (1991)
16. Inoue, A., Amiya, K., Yoshii, I., Kimura, H.M., Masumoto, T.: Production of Al-based amorphous alloy wires with high tensile strength by a melt extraction method. *Mater. Trans. JIM* **35**, 485–488 (1994)
17. Maringer, R.E., Mobley, C.E.: Casting of metallic filament and wire. *J. Vac. Sci. Technol.* **11**, 1067 (1974)
18. Allahverdi, M., Drew, R.A.L., Rudkowska, P., Rudkowski, G., Strom-Olsen, J.O.: Amorphous CaO-Al<sub>2</sub>O<sub>3</sub> wires by melt extraction. *Mater. Sci. Eng. Struct. Mater. Prop. Microstruct. Process.* **A207**, 12–21 (1996)
19. Shen, T.D., Schwarz, R.B.: Lowering critical cooling rate for forming bulk metallic glass. *Appl. Phys. Lett.* **88**, 091903 (2006)
20. Allahverdi, M., Drew, R., Strom-Olsen, J.: Wetting and melt extraction characteristics of ZrO<sub>2</sub>-Al<sub>2</sub>O<sub>3</sub> based materials. *J. Am. Ceram. Soc.* **80**, 2910–2916 (1997)
21. Maringer, R.E., Mobley, C.E.: Melt extraction of metallic filament and staple wire. *AIChE Symp. Ser.* **74**, 16–19 (1978)
22. Engineering, M.: Fine metallic and ceramic wires by melt extraction. *Techniques* **1**, 158–162 (1994)
23. Baik, N.I., Choi, Y., Kim, K.Y.: Fabrication of stainless steel and aluminum wires by PDME method. *J. Mater. Process. Technol.* **168**, 62–67 (2005)
24. Arkhangel'skij, V.M., Mitin, B.S.: Problems in wire producing by pendant drop melt extraction. *Stal'*, 71–76 (2001)
25. Archangelsky, W., Prischepov, S.V., Vasiliev, V.A.: Adhesion interaction on melt extraction from pendant drop. *Mater. Sci. Eng. A Struct. Mater. Prop. Microstruct. Process.* **304**, 598–603 (2001)
26. Strom-Olsen, J.: Fine fibres by melt extraction. *Mater. Sci. Eng. A Struct. Mater. Prop. Microstruct. Process.* **A178**, 239–243 (1994)
27. Allahverdi, M., Drew, R.A.L., Strom-Olsen, J.: Melt extraction and properties of ZrO<sub>2</sub> · Al<sub>2</sub>O<sub>3</sub>-based wires. *Ceram. Eng. Sci. Proc.* **16**, 1015–1025 (1995)
28. Rudkowski, P., Strom-Olsen, J.O., Rudkowska, G., Zaluska, A., Ciureanu, P.: Ultra fine, ultra soft metallic fibres. *IEEE Trans. Magn.* **31**, 1224–1228 (1995)
29. Allahverdi, M., Drew, R.A.L., Strom-Olsen, J.O.: Melt-extracted oxide ceramic fibres - The fundamentals. *J. Mater. Sci.* **31**, 1035–1042 (1996)
30. Allahverdi, M., Drew, R.A.L., Strom-Olsen, J.O.: Wetting and melt extraction characteristics of ZrO<sub>2</sub>-Al<sub>2</sub>O<sub>3</sub> based materials. *J. Am. Ceram. Soc.* **80**, 2910–2916 (1997)
31. Strom-olsen, J.O., Rudkowska, G., Rudkowski, P., Allahverdi, M., L. Drew, R.A. Fine metallic and ceramic fibres by melt extraction. *Mater. Sci. Eng. A Struct. Mater. Prop. Microstruct. Process.* **179–180**, 158–162 (1994)
32. Katsuya, A., Inoue, A., Masumoto, T.: Production and properties of amorphous alloy wires in Fe-B base system by a melt extraction method. *Mater. Sci. Eng. A Struct. Mater. Prop. Microstruct. Process.* **226**, 104–107 (1997)
33. Zhang, T., Inoue, A.: A new method for producing amorphous alloy wires. *Mater. Trans. JIM* **41**, 1463–1466 (2000)
34. Inoue, A., Amiya, K., Katsuya, A., Masumoto, T.: Mechanical properties and thermal stability of Ti- and Al-based amorphous wires prepared by a melt extraction method. *Mater. Trans. JIM* **36**, 858–865 (1995)
35. Taha, M.A., El-Mahallawy, N.A., Abdel-Gaffar, M.F.: Geometry of melt-spun ribbons. *Mater. Sci. Eng. A* **A134**, 1162–1165 (1991)
36. Tanner, B.R.I.: Note on the Rayleigh Problem for a Visco-Elastic Fluid. **13**, 573–580 (1962)
37. Saasen, B.A., Tyvand, P.A.: Rayleigh-Taylor instability and Rayleigh-type waves on a Maxwell-fluid. *J. Appl. Math.* **41**, 284–293 (1990)

38. Olson, B.J., Cook, A.W.: Rayleigh-Taylor shock waves. *Phys. Fluids* **19**, 128108 (2007)
39. Akihisa, I.: Preparation of amorphous Fe-Si-B and Co-Si-B alloy wires by a melt extraction method and their mechanical and magnetic properties. *Mater. Trans.* **36**, 802–809 (1995)
40. Allahverdi, M., Drew, R.A.L., Rudkowska, P., Rudkowski, G., Strom-Olsen, J.O.: Amorphous  $\text{CaO} \cdot \text{Al}_2\text{O}_3$  wires by melt extraction. *Mater. Sci. Eng. A Struct. Mater. Prop. Microstruct. Process.* **207**, 12–21 (1996)
41. Kavesh, S.: Melt spinning of metal wires. *AIChE Symp. Ser.* **74**, 1–15 (1978)
42. Schlichting, H., Gersten, K.: *Boundary-Layer Theory*, Berlin: Springer Verlag, (2000)
43. Schlichting, H.: *Theory of Boundary Layer*. Nauka, Moscow (1969)
44. Wang, H., Qin, F.X., Xing, D.W., et al.: Fabrication and characterization of nano/amorphous dualphase FINEMET microwires. *Mater. Sci. Eng. B* **178**(20), 1483–1490 (2013)
45. Khandogina, E.N., Petelin, A.L.: Magnetic, mechanical properties and structure of amorphous glass coated microwires. *J. Magn. Magn. Mater.* **249**, 55–59 (2002)
46. Qin, F.X., et al.: Mechanical and magnetocaloric properties of Gd-based amorphous microwires fabricated by melt-extraction. *Acta Mater.* **61**, 1284–1293 (2013)
47. Mukai, T., Nieh, T.G., Kawamura, Y., Inoue, A., Higashi, K.: Effect of strain rate on compressive behavior of a  $\text{Pd}_{40}\text{Ni}_{40}\text{P}_{20}$  bulk metallic glass. *Intermetallics* **10**, 1071–1077 (2002)
48. Spaepen, F.: A microscopic mechanism for steady state inhomogeneous flow in metallic glasses. *Acta Metall.* **25**, 407–415 (1977)
49. Wu, F.F., Zhang, Z.F., Mao, S.X.: Size-dependent shear fracture and global tensile plasticity of metallic glasses. *Acta Mater.* **57**, 257–266 (2009)
50. Wang, H., et al.: Relating residual stress and microstructure to mechanical and giant magneto-impedance properties in cold-drawn Co-based amorphous microwires. *Acta Mater.* **60**, 5425–5436 (2012)
51. Yi, J., et al.: Micro-and nanoscale metallic glassy wires. *Adv. Eng. Mater.* **12**, 1117–1122
52. Nagase, T., Kinoshita, K., Nakano, T., Umakoshi, Y.: Fabrication of Ti-Zr binary metallic wire by Arc-Melt-Type melt-extraction method. *Mater. Trans.* **50**, 872–878 (2009)
53. Takayama, S.: Drawing of  $\text{Pd}_{77}\text{Cu}_6\text{Si}_{16}$  metallic glass wires. *Mater. Sci. Eng.* **38**, 41–48 (1979)
54. Masumoto, T., Ohnaka, I., Inoue, A., Hagiwara, M.: Production of Pd-Cu-Si amorphous wires by melt spinning method using rotating water. *Scripta Metall* **15**, 293–296 (1981)
55. Zberg, B., Arata, E.R., Uggowitzer, P.J., Lofler, J.F.: Tensile properties of glassy MgZnCa wires and reliability analysis using Weibull statistics. *Acta Mater.* **57**, 3223–3231 (2009)
56. Nagase, T., Ueda, M., Umakoshi, Y.: Preparation of Ni-Nb-based metallic glass wires by arc-melt-type melt-extraction method. *J. Alloys Compd.* **485**, 304–312 (2009)
57. Metals, O., Centre, D.: Production of Ni-Pd-Si and Ni-Pd-P amorphous wires and their mechanical and corrosion properties. *Development* **20**, 97–104 (1985)
58. Wu, Y., et al.: Nonlinear tensile deformation behavior of small-sized metallic glasses. *Scr. Mater.* **61**, 564–567 (2009)
59. Vázquez, M.: Advanced magnetic microwires. In: *Handbook of Magnetism and Advanced Magnetic Materials*, vols 1–34. John Wiley & Sons, Ltd (2007)
60. Antonov, A.S., Borisov, V.T., Borisov, O.V., Prokoshin, A.F., Usov, N.A.: Residual quenching stresses in glass-coated amorphous ferromagnetic microwires. *J. Phys. D Appl. Phys.* **33**, 1161 (2000)
61. Zhang, S.L., Sun, J.F., Xing, D.W., Qin, F.X., Peng, H.X.: Large GMI effect in Co-rich amorphous wire by tensile stress. *J. Magn. Magn. Mater.* **323**, 3018–3021 (2011)
62. Antonov, A.S., et al.: Residual quenching stresses in amorphous ferromagnetic wires produced by an in-rotating-water spinning process. *J. Phys. D Appl. Phys.* **32**, 1788–1794 (1999)
63. Wu, Y., Wu, H.H., Hui, X.D., Chen, G.L., Lu, Z.P.: Effects of drawing on the tensile fracture strength and its reliability of small-sized metallic glasses. *Acta Mater.* **58**, 2564–2576 (2010)
64. Provenzano, V., Shapiro, A.J., Shull, R.D.: Erratum Reduction of hysteresis losses in the magnetic refrigerant  $\text{Gd}_5\text{Ge}_2\text{Si}_2$  by the addition of iron. *Nature* **435**, 528–528 (2005)

65. Jeong, S.: AMR (Active Magnetic Regenerative) refrigeration for low temperature. *Cryogenics* **62**, 193–201 (2014)
66. Dong, J.D., Yan, A.R., Liu, J.: Microstructure and magnetocaloric properties of melt-extracted La–Fe–Si microwires. *J. Magn. Magn. Mater.* **357**, 73–76 (2014)